



SAPIENZA
UNIVERSITÀ DI ROMA

Calibration of the MEGII drift chamber

Laurea Magistrale

Corso di Laurea in Fisica Nucleare e Subnucleare

Candidate

Anastasio Fratangelo

ID number 1530618

Thesis Advisors

Prof. Gianluca Cavoto

Prof. Cecilia Voena

Academic Year 2017/2018

Thesis not yet defended

Calibration of the MEGII drift chamber

Bachelor's thesis. Sapienza – University of Rome

© 2018 Anastasio Fratangelo. All rights reserved

This thesis has been typeset by L^AT_EX and the Sapthesis class.

Author's email: fratangelo.1530618@studenti.uniroma1.it

Contents

Introduction	v
1 Physics motivation	1
1.1 Muon decay in the Standard Model	2
1.2 Research of New Physics with $\mu \rightarrow e\gamma$	7
1.3 History of the $\mu \rightarrow e\gamma$ search	8
1.4 Search for other charged Lepton Flavor Violation processes	8
1.4.1 τ channel	10
2 The MEGII Experiment	11
2.1 Signal and background	13
2.1.1 Signal	13
2.1.2 Background	14
2.2 Beamline	15
2.3 Photon Detector	18
2.4 COBRA Magnet	21
2.5 Timing Counter	21
2.6 Radiative Decay Counter	23
2.7 Cylindrical Drift Chamber	26
2.8 DAQ System	28
2.9 MEGII expected performances	30
3 Event Reconstruction	31
3.1 Positron Reconstruction	31
3.1.1 DCH Waveform analysis	32
3.2 Photon Reconstruction	34
3.2.1 Waveform analysis	34
3.2.2 Photon position reconstruction	34
3.2.3 Photon timing reconstruction	35
3.2.4 Photon energy reconstruction	35
4 Drift Chamber Time Calibration	37
4.1 Time Calibration methods	38
4.1.1 Monte Carlo simulation	38
4.1.2 Template fit	40
4.1.3 Constant fraction method	41
4.2 Monte Carlo events analysis	42

4.2.1	Template fit Monte Carlo events	42
4.2.2	Constant fraction method Monte Carlo events	47
5	Drift Chamber z Calibration	51
5.1	Method	53
5.2	Monte Carlo analysis	55
6	Data Analysis	61
6.1	Monitoring Drift Chamber	61
6.2	Method	62
6.3	Results	63
7	Conclusions	67
A	Template fit parameters: samples of $2.5 \cdot 10^4$ and $5 \cdot 10^4$ signal events.	69
B	Template fit parameters distributions	71
C	Constant fraction method parameters distributions	75
D	Drift time distribution from the gas monitoring drift chamber.	77
	Bibliography	80

Introduction

The purpose of this thesis is to develop the algorithms of time and z coordinate calibration for the MEGII drift chamber. The MEGII experiment, placed in Switzerland, is the upgrade of the MEG experiment, which purpose is the search for the $\mu \rightarrow e\gamma$. A completely new drift chamber has been built for the upgrade. The MEGII drift chamber is a unique volume low-mass detector and it is composed by 1920 drift cells. The signal from the wires are amplified at each end and digitized by a custom board, the WaveDREAM, based on the DRS chip. The waveforms are then analyzed and its associated time and charge are extracted. From the time and charge at the two wire ends, the time and the longitudinal coordinate along the wire of the positron hit are determined. A calibration to correct for possible differences among the different electronic channels is necessary. The precision of the used algorithms needs to be verified in order not to affect the used methods.

The analysis here presented can be divided in three parts: the study of different algorithms for the time calibration constants, the charge calibration and a test of the time calibration on cosmic muon data taken with the MEGII gas monitoring chamber.

In the first part, two different algorithms are investigated for the determination of the time calibration constants: a template fit method and a constant fraction method are studied using Monte Carlo simulated events. In the end, the constant fraction method is chosen, and the data acquisition time necessary to collect a statistic to obtain the required precision on the calibration constant is determined.

In the second part, the study of the charge division method for the measure of the hit position along the wires is performed with Monte Carlo simulated events. In the third part, a cosmic muons data sample collected with the gas monitoring drift chamber of the MEGII experiment is used to test the constant fraction method. The time distribution of the different channels of the monitoring drift chamber are aligned.

In the first chapter, the theoretical background and the history of the search for $\mu \rightarrow e\gamma$ are explained and compared with other cLFV researches. In the second chapter, all the MEGII detectors and the front-end electronics are presented paying particular attention to the new drift chamber. In the third chapter, the waveform analysis is explained focusing on the drift chamber waveform analysis. The fourth and fifth chapters show the analysis developed respectively for the time and charge calibration. The algorithms and the methods are explained showing the obtained results with Monte Carlo simulated events. In the sixth chapter, the time calibration has been tested using the cosmic muon data from the MEGII gas monitoring drift chamber.

Chapter 1

Physics motivation

The Standard Model (SM) of particle physics is based on a gauge theory of the strong and electroweak interactions $SU(3) \otimes SU(2) \otimes U(1)$. Since it was established, the SM has been successfully tested with a large number of experiments. Although many phenomena are explained with the current model, there are many aspects of the elementary particle physics which remain not explained, as for example the origin of the dark matter and the neutrino mass. The presence of these not fully understood phenomena suggests that the SM could be an approximation of a wide and more complex theory, which explains all the fundamental interactions. There are many Beyond Standard Model (BSM) theories that are extension of the SM. Even if many experiments are searching for the evidence of new physics, up to now this has not been discovered yet. The direct searches of new particles introduced by new symmetries in BSM is limited by present collider technology but it is also possible to realize indirect searches of new physics. One of the most powerful methods to search for BSM is looking for charged lepton flavor violation (cLFV).

In the first part of this chapter, the theoretical background is briefly presented and, in the second part, some of the past experiments, which were searching for cLFV are reported with their results.

1.1 Muon decay in the Standard Model

In the SM there are two kinds of particles: bosons and fermions. The bosons mediate the fundamental interactions: electromagnetism, weak and strong interactions. For each interaction, one or more gauge bosons exist: the gluon g is the carrier of the strong interaction, the W^\pm and the Z^0 mediate the weak interaction and the photon γ the electromagnetism. Moreover, there are fermions that are separated into two categories: quarks and leptons. There exist six different quarks and six different

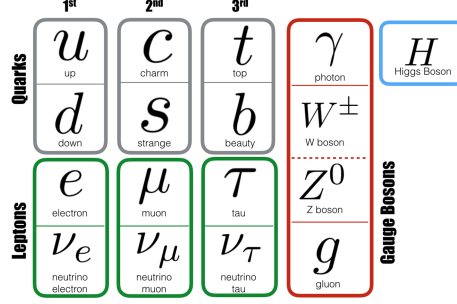


Figure 1.1. Elementary particles in the SM.

leptons. They are divided in three generations each of them containing a quark doublet and a lepton doublet. In the lepton doublet, there is a neutrino associated with a charged lepton. Differently from quarks, which can interact via all the three fundamental forces, the leptons can interact only via the electromagnetic and weak interactions. All the elementary particles are summarized in Figure 1.1.

Thanks to the gauge symmetries, it is possible to write the lagrangian of the SM in which all the interactions are described. This lagrangian explains how fermions and bosons interact with each other. The SM lagrangian includes different terms from which the different interactions can be derived. A flavor quantum number is associated with each quark and lepton that characterizes the weak interaction. The flavor sector for the leptons in the SM arises from the Yukawa couplings of the fermion fields with the Higgs field Φ :

$$-L_Y = (Y_u)_{ij} \bar{Q}_{Li} u_{Rj} \tilde{\Phi} + (Y_d)_{ij} \bar{Q}_{Li} d_{Rj} \Phi + (Y_e)_{ij} \bar{L}_{Li} e_{Rj} \Phi + h.c. \quad (1.1)$$

where $SU(2)_L$ indices were omitted, i and j run over the three families and Y_f ($f = u, d, e$) are in general complex matrices 3×3 . The fields defined as Q_L are the left-handed quark doublets, u_R and d_R are the right-handed quark up and down, L_L is the left-handed lepton doublets and e_R the right-handed leptons.

In the original formulation of the SM, the neutrinos are exactly massless. The Yukawa matrices, and thus the fermion mass matrices, can be diagonalized by unitary rotations of the fields. Because of the unitarity of the transformations, the kinetic terms and neutral current of the lagrangian are not modified. The fermion couplings to the Higgs are proportional to the mass matrix, thus they can be diagonalized in the same basis. This means that flavor is conserved.

On the other hand, in the charged-current interactions with the W bosons, we find:

$$L_{CC} = \frac{g}{\sqrt{2}} (\bar{u}_L \gamma^\mu (V_u^\dagger V_d) d_L + \bar{\nu}_L \gamma^\mu (V_\nu^\dagger V_e) e_L) W_\mu^+ + h.c. \quad (1.2)$$

It can be noticed that the flavor violation in quark sector is due to the diagonalization of the Y_u and Y_d that requires $V_u \neq V_d$. The term $V_u^\dagger V_d$ represents the Cabibbo-Kobayashi-Maskawa matrix V_{CKM} that describes the flavor change phenomena.

In the lepton sector of the original SM with massless neutrinos, the leptonic flavor is exactly conserved because of the term V_ν which can be chosen equal to V_e . In fact, in this configuration no other term in the Lagrangian involves the doublets.

These considerations are not correct in the case of massive neutrinos. In fact, the observation of the neutrino oscillations [1] implies the necessity of an extension of the original SM to include neutrino mass terms. This means that the lepton family numbers are not conserved. In this configuration, diagonalizing the charged lepton and neutrino mass terms, a matrix is introduced to describe the lepton flavor violation just like the CKM matrix. This is the Pontecorvo-Maki-Nakagawa-Sakata (PMNS) matrix. The neutrino oscillations are due to the neutrino flavor eigenstates and mass eigenstates, which are not the same. The flavor eigenstates are observable in the weak interactions. For this reason, the neutrino flavor eigenstates can be written as a linear combination of the neutrino mass eigenstates, as follow:

$$\nu_\alpha = \sum_{k=1,3} U_{\alpha k} \nu_k \quad \alpha = e, \mu, \tau. \quad (1.3)$$

Starting from this, we can determine the neutrino oscillation probability. For example, if we consider only two neutrinos, ν_e and ν_μ , with two mass eigenstates ν_1 and ν_2 , the initial state of ν_μ is:

$$|\nu_\mu(t=0)\rangle = -\sin\theta |\nu_1\rangle + \cos\theta |\nu_2\rangle \quad (1.4)$$

where θ is the mixing angle. The flavor eigenstate evolved after a time t is:

$$|\nu_\mu(t)\rangle = -\sin\theta e^{-iE_1 t} |\nu_1\rangle + \cos\theta e^{-iE_2 t} |\nu_2\rangle \quad (1.5)$$

It is possible to determine the probability that after a time t the initial ν_μ becomes ν_e :

$$P(\nu_\mu \rightarrow \nu_e, t) = |\langle \nu_e(t) | \nu_\mu(t=0) \rangle|^2 \quad (1.6)$$

Which results:

$$P(\nu_\mu \rightarrow \nu_e, t) = \sin^2(2\theta) \sin^2\left(\frac{\Delta m^2}{4E} t\right) \quad (1.7)$$

where $\Delta m^2 = m_2^2 - m_1^2$.

It is useful to introduce the *branching ratio* (BR) of decay as:

$$BR = \frac{\Gamma_i}{\Gamma} \quad (1.8)$$

where Γ_i is the width of a decay mode i and Γ is the total width. The principal muon decays is $\mu^- \rightarrow e^- \nu_\mu \bar{\nu}_e$, this process has a $BR(\mu^- \rightarrow e^- \nu_\mu \bar{\nu}_e) = \Gamma(\mu^- \rightarrow e^- \nu_\mu \bar{\nu}_e) / \Gamma_{tot} \approx 100\%$ [2]. The Feynmann diagram for this decay is reported in Figure 1.2.

This process is called *Michel Decay* and it is described by the following Hamiltonian

$$H = -\frac{G_F}{\sqrt{2}} \bar{u}(P_{\nu_\mu}) \gamma^\mu (1 - \gamma^5) u(P_\mu) \bar{u}(P_e) \gamma_\mu (1 - \gamma_5) u(P_{\nu_e}) \quad (1.9)$$

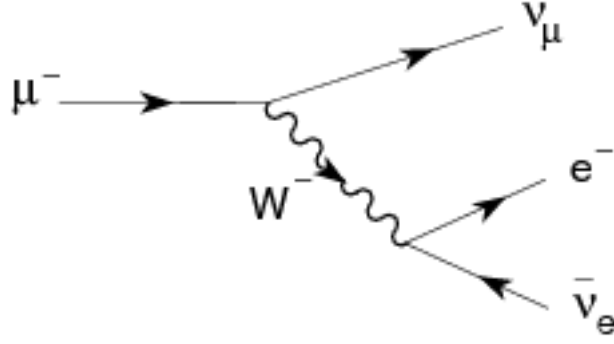


Figure 1.2. Feynmann diagram of muon Michel decay.

where G_F is the Fermi constant, $\bar{u}(P), u(P)$ are the Dirac spinors and γ^μ, γ^5 are the Dirac matrices and P is the four-momentum.

It is useful to determine the matrix element M_{if} of the transition from the initial state $i = \mu$ to the final $f = e, \bar{\nu}_e, \nu_\mu$,

$$|M_{if}|^2 = |\langle e, \bar{\nu}_e, \nu_\mu | H | \nu_\mu \rangle|^2 \quad (1.10)$$

The differential decay rate results as:

$$d\Gamma = \frac{1}{2m_\mu} \frac{1}{2} \sum_{pol} |M_{if}|^2 (2\pi)^4 \delta^4(P_\mu - P_{\nu_\mu} - P_e - P_{\bar{\nu}_e}) \frac{dP_e}{(2\pi)^3} \frac{dP_{\nu_\mu}}{(2\pi)^3} \frac{dP_{\bar{\nu}_e}}{(2\pi)^3} \quad (1.11)$$

where the average over the spins of the initial state and the sum over the polarizations of the final state have been calculated. The $\delta^4(\dots)$ represents the conservation of the four-momenta and the terms $\frac{dP_e}{(2\pi)^3} \frac{dP_{\nu_\mu}}{(2\pi)^3} \frac{dP_{\bar{\nu}_e}}{(2\pi)^3}$ are the infinitesimal volume in the phase space.

To determine the rate of the Michel decay it is necessary to compute the element of the matrix $|M_{if}|^2$ and to integrate over the phase space of the final state particles considering the conservation of the four-momenta. Using the properties of the γ matrices and considering the energies and masses of the involved particles, the Michel decay can be computed as a point-like decay ignoring the mass of the particles. In this configuration, the matrix element results to be:

$$|M_{if}|^2 = 128G_F^2(P_\mu \cdot P_{\nu_e})(P_e \cdot P_{\nu_\mu}) \quad (1.12)$$

And finally the $\Gamma(\mu \rightarrow e\bar{\nu}_e\nu_\mu)$ is:

$$\Gamma(\mu \rightarrow e\bar{\nu}_e\nu_\mu) = \frac{m_\mu^5 G_F^2}{192\pi^3} \quad (1.13)$$

with the muon mass $m_\mu = 105.66 \text{ MeV}$, mean life $\tau_\mu = (2.1969811 \pm 0.0000022) \cdot 10^{-6} \text{ s}$ [2]. Another possible muon decay mode is the Radiative Muon decay (RMD) which is similar to the Michel decay but in the final state, together with the electron and the two neutrinos, there is the emission of a photon

$$\mu \rightarrow e\bar{\nu}_e\nu_\mu\gamma \quad (1.14)$$

All the principal muon decay modes are reported with the corresponding BR in the Table 1.1 together with the not yet observed cLFV decay modes.

	Mode	Fraction (Γ_i/Γ)	Confidence level
Γ_1	$e^- \bar{\nu}_e \nu_\mu$	$\approx 100\%$	
Γ_2	$e^- \bar{\nu}_e \nu_\mu \gamma$	$(1.4 \pm 0.4)\%$	
Γ_3	$e^- \bar{\nu}_e \nu_\mu e^+ e^-$	$(3.4 \pm 0.4) \cdot 10^{-5}$	
Γ_4	$e^- \nu_e \bar{\nu}_\mu$	$< 1.2\%$	90%
Γ_5	$e^- \gamma$	$< 5.7 \cdot 10^{-13}$	90%
Γ_6	$e^- e^+ e^-$	$< 1.0 \cdot 10^{-12}$	90%
Γ_7	$3e^- 2\gamma$	$< 7.2 \cdot 10^{-11}$	90%

Table 1.1. Muon decay modes in the SM with respective BR. The last four decays are upper limit on the lepton family number violating modes [2].

The SM Feynmann diagram for $\mu \rightarrow e\gamma$ decay is shown in Figure 1.3.

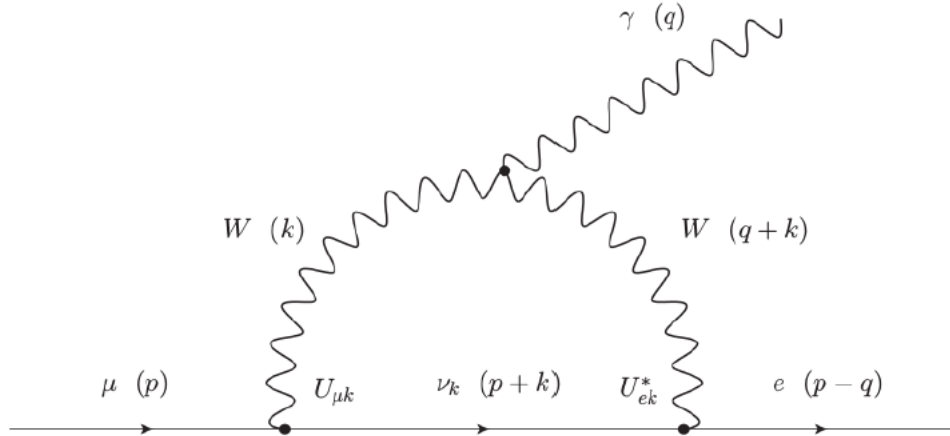


Figure 1.3. Feynmann diagram of $\mu \rightarrow e\gamma$ in the SM with massive neutrinos. The four-momenta of the particle are indicated in parenthesis.

The process can happen only through the neutrino oscillation $\nu_\mu \rightarrow \nu_e$ and the decay amplitude is given by the matrix element:

$$M(\mu \rightarrow e\gamma) = i\bar{u}_e(p-q)V_\alpha u_\mu(p)\epsilon^{*\alpha}(q) \quad (1.15)$$

where p and q are the four-momenta of the muon and of the photon, u_e and u_μ are the Dirac spinors for the electron and the muon, ϵ^α the polarization vector of the photon. V_α is the operator that describes this transition and it can be written in terms of Lorentz-invariant amplitudes F_i :

$$V_\alpha = \sigma_{\alpha\beta} q^\beta (F_1 + F_2 \gamma_5) + \gamma_\alpha (F_3 + F_4 \gamma_5) + q_\alpha (F_5 + F_6 \gamma_5) \quad (1.16)$$

where $\sigma_{\alpha\beta} = \frac{i}{2}[\gamma_\alpha, \gamma_\beta]$.

Using the properties of the gamma matrices, considering $m_e \ll m_\mu$, it results:

$$|M|^2 = m_\mu^4(|A_R|^2 + |A_L|^2) \quad (1.17)$$

with $A_{R,L} = F_1 \pm F_2$. The resulting decay rate is:

$$\Gamma(\mu \rightarrow e\gamma) = \frac{|M|^2}{16\pi m_\mu} = \frac{m_\mu^3}{16\pi}(|A_R|^2 + |A_L|^2) \quad (1.18)$$

Computing the two terms A_R, A_L , $A_R \propto m_\mu$ and $A_L \propto m_e$, thus $|A_L|^2 \ll |A_R|^2$. This means that there is no need to compute the $|A_L|^2$, whereas the other term is:

$$A_R = \frac{g^2 e}{128\pi^2} \frac{m_\mu}{M_W^4} \sum_{k=1,3} U_{\mu k} U_{ek}^* m_{\nu_k}^2.$$

Finally the $BR(\mu \rightarrow e\gamma)$ obtained is:

$$BR(\mu \rightarrow e\gamma) \simeq \frac{\Gamma(\mu \rightarrow e\gamma)}{\Gamma(\mu \rightarrow e\bar{\nu}_e, \nu_\mu)} = \frac{3\alpha}{32\pi} \left| \sum_{k=1,3} \frac{U_{\mu k} U_{ek}^* m_{\nu_k}^2}{M_W^2} \right|^2 \quad (1.19)$$

The BR value can be calculated and it is $BR \simeq 10^{-54}$ which is experimentally inaccessible.

1.2 Research of New Physics with $\mu \rightarrow e\gamma$

Even if the SM has been successfully proved and explains a wide variety of phenomena, it is considered a low-energy approximation of a more general theory. It has been seen how the $\mu \rightarrow e\gamma$ decay is an extremely low probability process in the SM. Any observation of this process is a clear signal of new physics. Many Beyond Standard Models (BSMs) predict that the $\mu \rightarrow e\gamma$ decay can happen in the detectable branching fraction. There is a large number of candidates for such theory and supersymmetric (SUSY) models are ones of these. SUSY introduces a new gauge symmetry called "supersymmetry" as an extension of the SM and, as a result, all the elementary SM particles have their own supersymmetric partner called sparticles. In the case of unbroken supersymmetry, each particle and its relative sparticle have the same mass. Actually, these supersymmetric particles have not yet been discovered. Another approach to the physics beyond SM is the Grand Unified Theory (GUT). In the GUT all the SM interactions are unified at the energy scale of $\mathcal{O}(10^{16})$ GeV. At this energy scale, all the three couplings constants of strong, weak and electromagnetic interactions are the same.

An interesting SUSY extension is given by the SUSY-GUT models, in which all the interactions are unified to a single $SU(5)$ gauge coupling constant. Considering the slepton mass matrix in the SUSY-GUT, the off-diagonal elements are given by

$$(m_{\tilde{e}_R}^2)_{ij} = -\frac{3}{8\pi^2}(V_R)_{i3}(V_R)_{j3}^*|y_u^{33}|^2m_0^2(3+|A_0^2|)\ln\left(\frac{M_P}{M_G}\right) \quad (1.20)$$

where V_R is a matrix element to diagonalize the Yukawa coupling for the lepton, M_P is the reduced Planck mass $\sim 2 \cdot 10^{18}$ GeV, M_G is the GUT scale $\sim 2 \cdot 10^{16}$ GeV, m_0 and A_0 are respectively the universal scalar mass and the universal coupling. The equation (1.20) predicts a source for the $\mu \rightarrow e\gamma$ decay and in Figure 1.4, two possible diagrams in the $SU(5)$ SUSY-GUT model for the $\mu \rightarrow e\gamma$ are shown. In

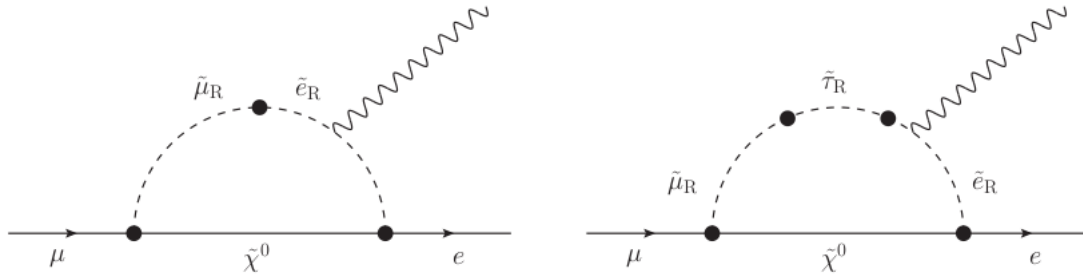


Figure 1.4. Possible diagrams for the $\mu \rightarrow e\gamma$ in the SUSY-GUT model.

this scenario, for a different parameters of the BSM models, the decay is expected to have a BR in the range between $10^{-11} - 10^{-15}$. The MEG Experiment already reached a good sensitivity and, as reported in Table 1.2, obtained the best upper limit on the BR with a confidence level of 90%. This is useful to put constraints on the parameters of the BSMs.

1.3 History of the $\mu \rightarrow e\gamma$ search

Since muons were discovered in 1936 by Carl Anderson at Caltech studying cosmic rays, they were considered really fascinating particles with some peculiar and interesting properties. In fact, after its discover, the muon was considered to be the candidate mediating the strong interaction, as predicted by Yukawa. The experiment performed in 1945 by Conversi, Pancini and Piccioni, demonstrated that the muon does not interact via strong force and for this, it was not the Yukawa meson.

In Figure 1.5 the three different stages of the $\mu \rightarrow e\gamma$ research are reported.

The first experiment on the search for the $\mu \rightarrow e\gamma$ decay has been performed by Hinks and Pontecorvo in 1947 [3]. They stopped cosmic ray muons using a lead absorber and measured the coincidence between signals from two Geiger-Muller counters. They did not observe any coincidence. For this reason, they put a limit on the decay rate, which was essentially the inverse of the number of the observed muons.

Until 70's, the limit on the process has been improved by the introduction of muons artificially produced by using stopped pion beams. Starting from the 70's, the pion beams have been substituted by muon beams and the sensitivity on the decay improved also thanks to constantly improving detector technologies. The decay has not been observed yet and the best upper limit on the BR was obtained at PSI with MEG experiment which finished its data analysis in 2016 [4]. In Table 1.2 all the experiments carried out from the 1977 until now are reported.

Year	Experiment	Beam Rate (Hz)	Upper Limit 90%C.L.	Ref.
1977	TRIUMF	$2 \cdot 10^5$	$3.6 \cdot 10^{-9}$	[5]
1980	SIN	$5 \cdot 10^5$	$1 \cdot 10^{-9}$	[6]
1982	E328	$2.4 \cdot 10^6$	$1.7 \cdot 10^{-10}$	[7]
1988	Crystal Box	$4 \cdot 10^5$	$4.9 \cdot 10^{-11}$	[8]
1999	MEGA	$2.5 \cdot 10^8$	$1.2 \cdot 10^{-11}$	[9]
2013	MEG	$3 \cdot 10^7$	$4.2 \cdot 10^{-13}$	[4]

Table 1.2. All the past experiments with their upper limit on the branching ratio of the $\mu \rightarrow e\gamma$ decay are reported.

1.4 Search for other charged Lepton Flavor Violation processes

The $\mu \rightarrow e\gamma$ is not the only channel used for the search of cLFV. Many experiments are looking for decays violating the lepton flavor in others channels.

Two interesting muons flavor violating processes are: $\mu^+ \rightarrow e^+e^-e^+$, $\mu^- N \rightarrow e^- N$ conversion. The BR of these processes is related to that of $\mu \rightarrow e\gamma$ in a model dependent way. In Figure 1.5 the history of the search for this three different decays is reported.

- $\mu^+ \rightarrow e^+e^-e^+$ decay is a three-body decay with a total energy in the final state equal to the muon mass. The two positrons and the electron are emitted in a common plane and each particles has a maximum momentum of about

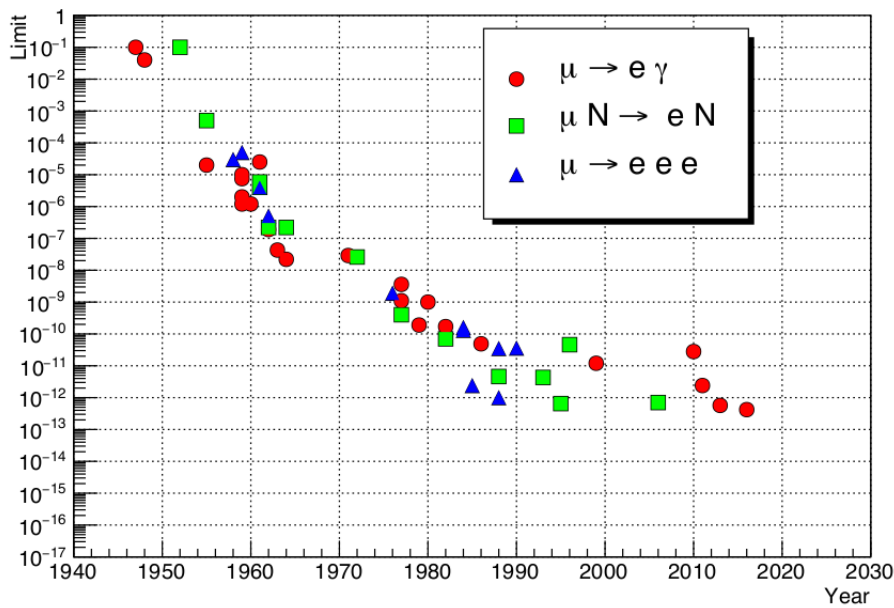


Figure 1.5. Limit on the branching ratio of flavor violating muon decays as a function of the year [10].

half of muon mass. The energy distribution of each produced particle depends on the exact dynamics of the unknown physics. The advantage of the research for this rare decay is that no photons and neutrinos are emitted. This implies that the only detector needed is an excellent tracker as thin as possible, which should reconstruct tracks with a momentum from a MeV up to half of the muon mass. The backgrounds are similar to those in $\mu \rightarrow e \gamma$ search. In fact, there is a prompt background due to the muon decay $\mu^+ \rightarrow e^+ e^- e^+ \bar{\nu}_\mu \nu_e$ with the two neutrinos carrying out a very little energy. The energy spectrum of this decay is similar to the Michel decay spectrum. The other background is due to the accidental overlay of two or three uncorrelated muons decay. This background can be suppressed with a precise measurement of the vertex and timing in addition to the energy measurement. The best upper limit on the BR up to now has been reached in 1988 by SINDRUM experiment at PSI [11]. In the 2019, the new experiment Mu3e at PSI should start its data-taking. The aim of Mu3e [12] is to reach a sensitivity of $\mathcal{O}(10^{-16})$.

- $\mu^- N \rightarrow e^- N$ conversion is a spontaneous decay of a muon to an electron without the emission of neutrinos, within the Coulomb potential of an atomic nucleus. It is possible only for the negative muons. If the conversion leaves the nucleus at its ground state, all the muon mass get into the kinetic energy of the electron and the recoil of the parent nucleus. The signature of this process is the production of monochromatic electron at an energy which is essentially the muon mass corrected for the binding energy and nuclear recoil. The principal sources of background are: μ^- decays in orbit (DIO), radiative muon capture (RMC), cosmic rays that interact in the detector material, muon decaying in flight that produce electrons in the kinematic signal region. Actually, the best

Chapter 2

The MEGII Experiment

The MEGII Experiment (Mu to Electron Gamma) is going to start its data taking in 2019 at Paul Scherrer Institute (PSI) in Switzerland. MEGII, schematically represented in Figure 2.1, is the upgrade of the MEG experiment that searched for the $\mu \rightarrow e\gamma$ decay at PSI. The MEGII goal is to improve the sensitivity on the $\mu \rightarrow e\gamma$ branching ratio, defined as the 90% upper limit that can be set if no signal is observed, by one order of magnitude with respect to MEG, thus reaching $\sim 6 \cdot 10^{-14}$ in three years of data taking (Figure 2.2).

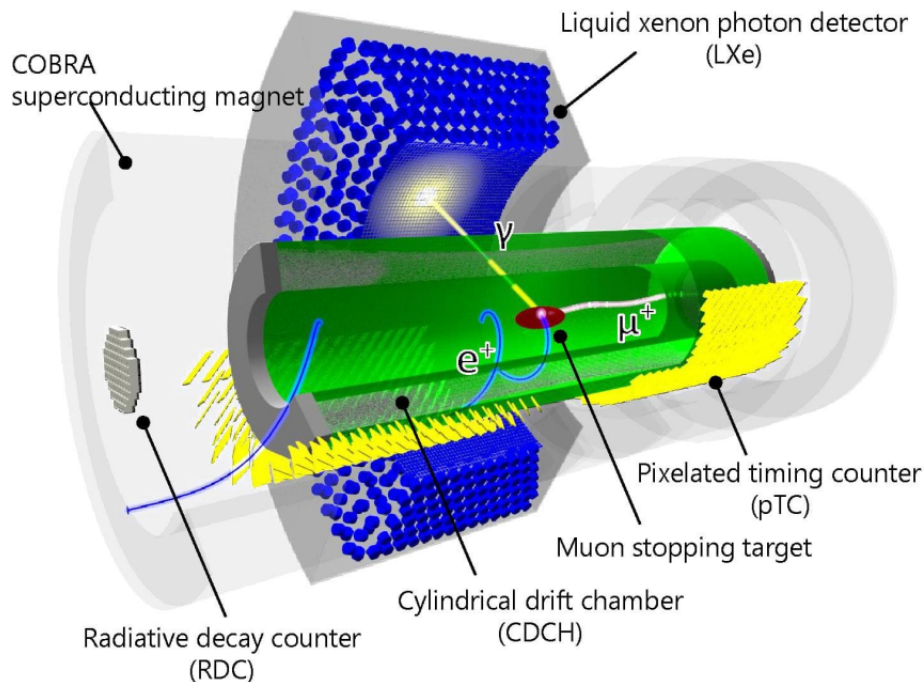


Figure 2.1. Schematic representation of the MEGII Experiment.

The MEGII Experiment aims to achieve the highest possible sensitivity using one of the world's most intense continuous surface muon beam (up to $\sim 10^8 \mu^+/s$). The muons are stopped in a target, thinner than the MEG one in order to reduce

the interactions of the outgoing positrons. The beam intensity is two times the value of the one used in MEG, i.e. $7 \cdot 10^7 \mu/s$, thus allowing to keep the accidental background at a sustainable level.

The MEGII experiment pursues the aim of the MEG Experiment renewing the detectors. The photon detector is an upgrade of the old detector, in fact, the calorimeter is the same C-shaped tank of 900 liters of liquid Xenon, but the 216 PMTs at the entrance face have been replaced by VUV-sensitive Multi-Pixel Photon Counter. The 16 old drift chamber (DCH) modules, used to track the positrons, have been replaced by a unique volume cylindrical detector with high granularity. The new drift chamber is placed inside the superconductive magnet (COBRA) which is the same of MEG. Inside COBRA, together with the drift chamber, there is a completely new timing counter (TC) that measures the positron time. The 30 plastic scintillation bars which composed the old timing counter have been substituted with 512 scintillation tiles. Finally, a Radiative Decay Counter (RDC) has been added to the experimental apparatus. The RDC is composed by plastic scintillators and LYSO bars and it is placed downstream of the drift chamber with respect to the direction of the upcoming muon beam.

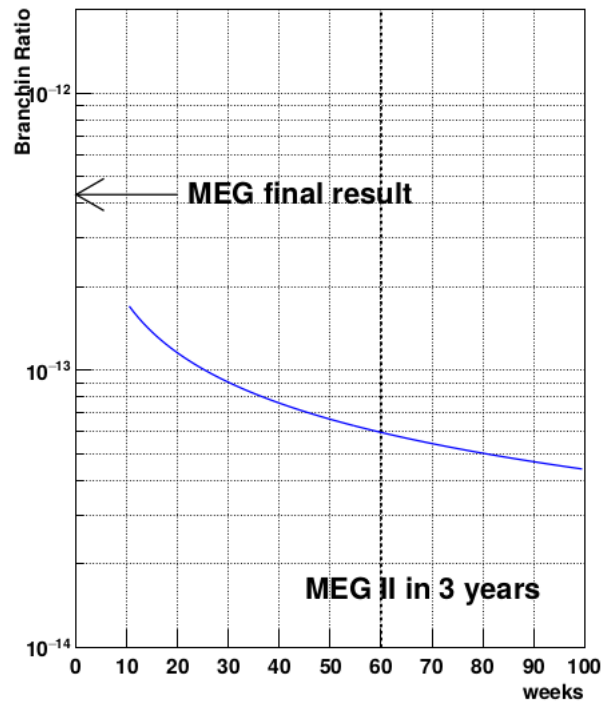


Figure 2.2. Expected sensitivity of MEGII as a function of data acquisition time.

In this chapter, the signature of the $\mu \rightarrow e\gamma$ decay is described and the different backgrounds of MEGII are discussed. After this, all the subdetectors are described with a particular attention to the DCH.

2.1 Signal and background

Any experiment needs a preliminary study of the signature of the signal and it is fundamental to know all the possible backgrounds before the realization of the detectors. In fact, this study is necessary in order to build the detectors with specific requirements and properties.

2.1.1 Signal

In an experiment such as MEG and MEGII, the signature of the $\mu \rightarrow e\gamma$ (Figure 2.3) is a two-body-decay since the muon is stopped and decays at rest. The characteristics

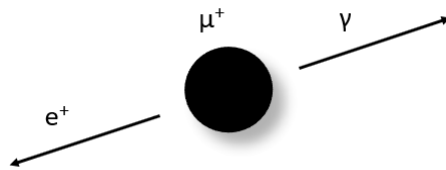


Figure 2.3. A schematic of $\mu^+ \rightarrow e^+\gamma$ decay with muon at rest.

of this decay are that the energy spectrum of both the particles produced is a Dirac delta function with energy equal to the half of the muon mass:

$$E_{e^+} = E_\gamma = \frac{m_\mu}{2} = 52.8 \text{ MeV} \quad (2.1)$$

where E_{e^+} and E_γ are respectively the energy of the positron and photon. The two particles are produced back-to-back and coincident in time:

$$\theta_{e\gamma} = 180^\circ, \quad t_{e+\gamma} = 0 \quad (2.2)$$

where $\theta_{e+\gamma}$ is the angle between the momentum of the e^+ and γ while $t_{e+\gamma}$ is the difference between their time of production.

These four variables are reconstructed to discriminate the signal against the background. The number of expected signal events N_{sig} is related to the branching ratio BR , to the muons stopping rate R_{μ^+} , the measurement time T , the solid angle Ω subtended by the photon and positron detectors, the efficiencies of the detectors ($\epsilon_{e^+}, \epsilon_\gamma$) and of the selection criteria ϵ_s . The relation between these variables is reported in Eq. 2.3.

$$N_{sig} = BR(\mu \rightarrow e\gamma) \times R_{\mu^+} \times \Omega \times T \times \epsilon_{e^+} \times \epsilon_\gamma \times \epsilon_s \quad (2.3)$$

It is useful to introduce the Single Event Sensitivity (SES) of an experiment, which is defined as the branching ratio such that the experiment would see one single event.

$$SES = \frac{1}{N_{sig}} \quad (2.4)$$

The goal is to obtain the lowest SES in order to be sensitive to the lowest possible value of BR and, for this, the largest possible R_{μ^+} is needed. Due to the presence of the background, it is not always convenient to increase R_{μ^+} as it will be discussed in the next subsection.

2.1.2 Background

The search for the $\mu \rightarrow e\gamma$ decay is complicated by two different types of background sources. The first one is the radiative muon decay (RMD) which is a prompt background. As already mentioned in the Section 1.1, in the RMD (Figure 2.4) together with a positron and two neutrinos there is a photon emitted. If the two

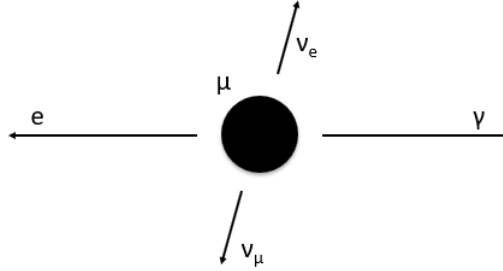


Figure 2.4. A schematic representation of radiative muon decay with two low-energy neutrinos.

neutrinos are produced with low-energy, the angle between the momentum of the positron and the photon is close to 180° and their energy is approximately equal to the signal one.

In fact, considering the variables $x = \frac{2E_e}{m_\mu}$, $y = \frac{2E_\gamma}{m_\mu}$ and $z = \pi - \theta_{e\gamma}$, the signal is represented by the case with $x = 1$, $y = 1$ and $z = 0$, but since every detector has a finite resolution there is an error δx and δy . The same thing on these quantities happens for the z that depends on the angular resolution δz . For detectors with good angular resolution, it can be assumed $\delta z \leq 2\sqrt{\delta x \delta y}$.

In Figure 2.5 there is the probability that prompt background can simulate the signal for different experimental resolutions. Once fixed the experimental resolution, it is possible to compute the contribution of the prompt background. For the MEG experiment, this contribution is evaluated to be lower than 10^{-14} , while for MEGII the prompt background contribution is expected to be lower than 10^{-16} .

The second type of background is given by the accidental coincidence of a positron from a Michel decay with a photon coming from a RMD, Bremsstrahlung or positron annihilation-in-flight (AIF). Figure 2.6 shows (a) the positron energy spectrum from an unpolarized Michel decay and (b) the gamma energy spectrum from RMD.

Integrating these two spectra it is possible to estimate the number of accidental background events:

$$N_{acc} \propto R_\mu^2 \times \Delta E_\gamma^2 \times \Delta p_{e^+} \times \Delta \theta_{e\gamma}^2 \times \Delta t_{e^+\gamma} \times T \quad (2.5)$$

where the Δ are the resolutions on the measured quantities and T is the acquisition time. The quadratic dependence from the photon energy derives from the integration of the photon spectrum. The quadratic dependence from the muon stopping rate implies that for fixed resolution it is not convenient to arbitrarily increase R_μ , but this should be chosen keeping in consideration the detector resolutions.

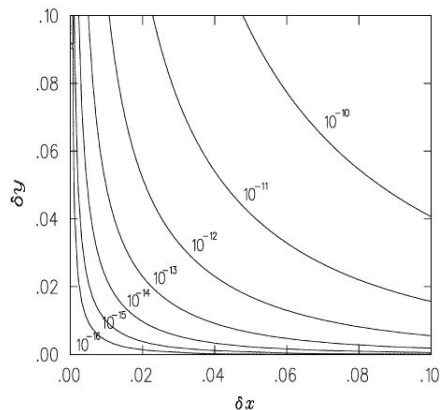


Figure 2.5. Probability that RMD simulate a signal event for different experimental resolution.

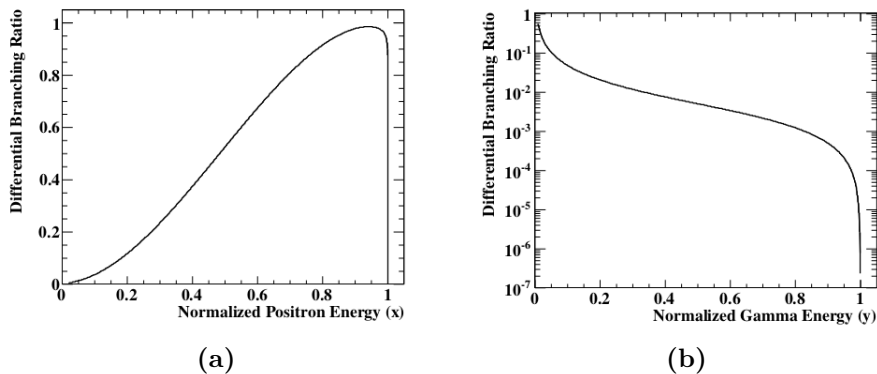


Figure 2.6. (a) Positron energy spectrum from unpolarized Michel decay. (b) Photon energy spectrum from radiative muon decay.

2.2 Beamline

The MEGII beamline components will be essentially the same of MEG. The proton ring cyclotron (Figure 2.7) at PSI generates a 590 MeV proton beam which frequency is 50.6 MHz . This frequency is high enough compared to the decay time of pions ($\tau_\pi \simeq 26 \text{ ns}$) and the muon beam can be considered continuous.

For this kind of experiments, positive muons are used in order to avoid nuclear capture by materials inside the target. The proton beam from the cyclotron interacts with a 4 cm thick graphite target producing π^+ and the pions decays producing the muons. The muons used for the experiment are only the *surface muons* that are those produced at the surface of the production target. The *surface muons* arrive monochromatic to the detectors through the channel called $\pi E5$. A schematic representation of $\pi E5$ beamline is reported in Figure 2.8. In the upstream of the $\pi E5$, surface muons are collected and are led at the center of the COBRA magnet. All these muons are fully polarized and have the same momentum of $28 \text{ MeV}/c$



Figure 2.7. Proton ring cyclotron at PSI.

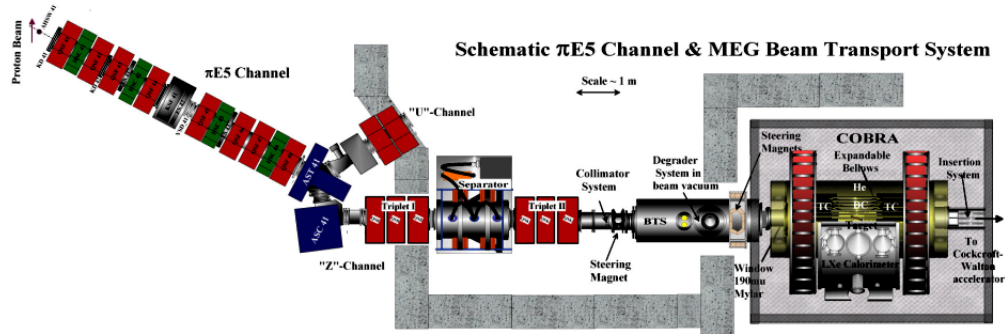


Figure 2.8. Schematic representation of the $\pi E5$ channel.

with 5 – 7% of spread in FWHM (Full Width at Half Maximum). For this reason, a high purity and high intensity muon beam can be selected. In order to separate the positron background and adjust the muon momentum a system of two quadrupoles, a Wien filter and a Beam Transport Solenoid (BTS) are used. At the center of the BTS, a $300 \mu\text{m}$ thick momentum degrader is placed to reduce the muons momentum and stop them in the target at the center of the detector.

It is important that the target has the following specific characteristics:

- a high muon stopping density
- allows reconstruction of the positron decay vertex
- minimization of multiple scattering for the outgoing positrons
- minimization of photon conversions from RMD
- minimization of positron AIF or Bremsstrahlung

In MEG the target was an elliptical $205 \mu\text{m}$ thick film of polyethylene-polyester. Several studies were performed to optimize the MEGII target. In the end the thickness and the angle between the target and the muon beam have been respectively

fixed at $140 \mu\text{m}$ and 15 degrees. The optimal target material has been studied and the polyethylene target has been chosen. In Figure 2.9 all the possibilities considered are reported.

Material	Degradar (μm)	Thickness (μm)	Thickness (X_0)	Inclination (deg)	Density (g cm^{-3})	Stop Efficiency (%)	Multiple Scattering (mrad)	
							μ^+ [18 MeV]	e^+ [52 MeV]
CH_2	350	140	2.8×10^{-4}	15.0	0.893	83	52.0	3.0
Be	350	90	2.6×10^{-4}	15.0	1.848	83	49.3	2.9
Mylar	350	100	3.5×10^{-4}	15.0	1.390	84	58.5	3.4
Scint. PVT	350	130	3.1×10^{-4}	15.0	1.032	84	54.5	3.2
Diamond	350	40	3.3×10^{-4}	15.0	3.515	81	56.8	3.3

Figure 2.9. Candidate target parameters with the corresponding performances.

For the polyethylene target (CH_2) the relative muon stopping efficiencies as a function of the thickness is reported in Figure 2.10.

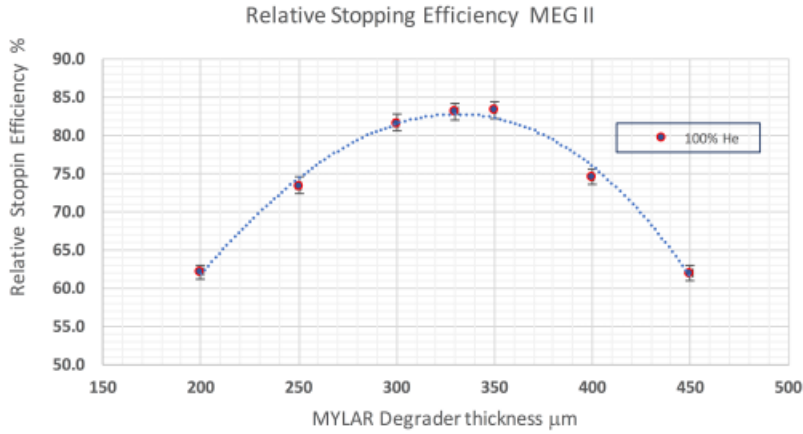


Figure 2.10. Simulation of the relative muon stopping efficiencies as a function of the polyethylene target thickness.

2.3 Photon Detector

The photon detector used in MEG was one of the world's biggest detectors based on the liquid Xenon (LXe) scintillation. The calorimeter is used to measure the energy, arrival time and interaction point of the photon. It is a C-shaped tank filled with 900l of LXe and surrounded by 846 PMT's (Photo Multiplier Tubes). The LXe has a fast decay time, short radiation length, high density and high detection efficiency. For the MEG calorimeter, the time resolution is measured to be about 67 ps, while the energy resolution depends on the photon conversion depth: 2.7% within 8 mm from the inner face, 2% between 8 mm and 3 cm and 1.7% for deeper conversion. In order to reach the best performances, the LXe has to work at a temperature around 165K and without any impurity. A high atomic number ($Z = 54$), combined with a high density in liquid phase ($\rho_{LXe} = 2.95 \text{ g/cm}^3$), make the liquid Xenon an excellent scintillator with a radiation length $X_0 = 2.77 \text{ cm}$. In the LXe about 20 eV are needed to have one scintillation photon. The photons are emitted by the Xe_2^* excimer de-excitation with wavelength of $\lambda = (175 \pm 5) \text{ nm}$, in the Vacuum UltraViolet (VUV) photons. In Figure 2.11 the principal characteristics of LXe are reported.

Atomic number	54
Atomic weight	131
Density at 161.35 K	2.978 g/cm ³
Radiation length	2.77 cm
Critical energy	10.5 MeV
Molier radius	4.1 cm
Boiling point	165 K
Melting point	161 K
Wavelength	178 nm
W_{ph} for electrons	21.6 eV
Decay time (recombination)	45 ns
Decay time (fast component)	4.2 ns
Decay time (slow component)	22 ns
Absorption length	>100 cm
Scatter length	29÷50 cm

Figure 2.11. Principal characteristics of liquid Xenon.

The cylindrical symmetry around the stopping target implies that the photons produced in the muons decay at rest, after they passed through the drift chamber and the central coil of the superconductive magnet, hit perpendicularly the inner face. The detector extends radially for 38.5 cm corresponding to $\sim 14 X_0$ and fully contains the γ -ray from a signal event. The inner radius of the detector is 67.85 cm, while the outer radius is 106.35 cm and the angular coverage is 12% of the solid angle.

One of the principal upgrade for the photon detector in MEGII is to reduce the areas in which photons could not be detected and to increase the read-out granularity. In order to obtain this, all the PMT's placed on the inner face have been substituted by smaller photo-sensors (Figure 2.12). Figure 2.13 shows an example

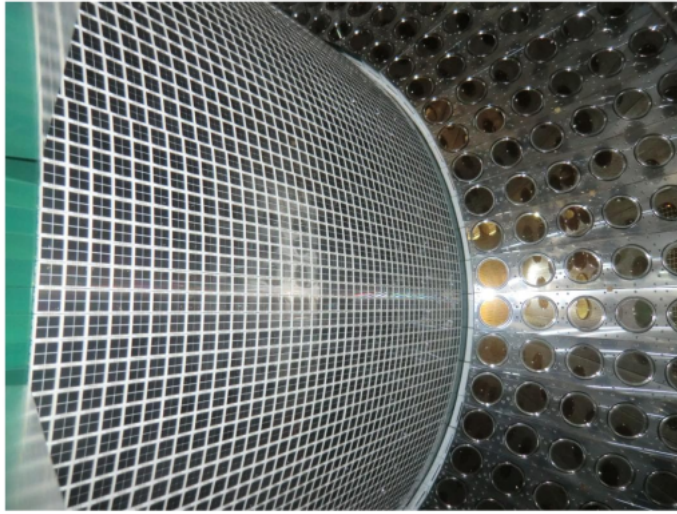


Figure 2.12. Picture of the LXe detector.

of scintillation light distribution read by PMTs on the entrance face on the left and the same distribution as it would appear with the upgraded detector on the right (from simulation). In particular, the new read-out allows a better separation

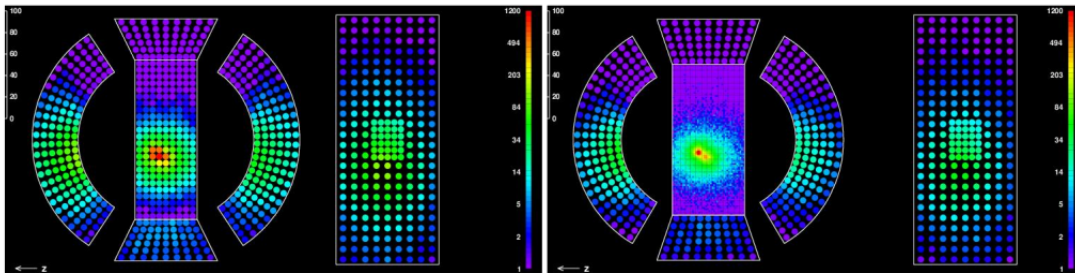


Figure 2.13. Example of scintillating light distributions PMT's on the left and read by photo-sensors on the right.

of pile-up photons. The photo-sensor is a Multi Pixel Photo Counter (MPPC) of $6 \times 6 \text{ mm}^2$. The MPPC is a photon counting device that is part of the SiPM family (Silicon PhotoMultiplier). There are a total of 4092 MPPC's on the inner face. The gain and quantum efficiencies parameter have been measured for each PMT. The absolute gain G is measured using 12 LEDs located on the lateral faces in order to illuminate all the PMTs. It is measured from the ratio of mean and statistical fluctuation of the output charge of the signal of the PMTs. The other measured parameter is the product of the quantum efficiency and collection efficiency, ϵ , which is calculated from the ratio of the output of each PMT in α source events. The Photo Detection Efficiency (PDE) for each MPPC is estimated using the same α source and considering the ratio between the number of the detected number of photo-electrons and the expected number of incoming scintillation photons. Once these parameters are found, the energy calibration of the entire calorimeter is

performed. In particular, the calibration of the LXe detector at the signal photon energy is realized using photons from π^0 decays produced by the π^- charge exchange reaction in a liquid hydrogen target $\pi^- p \rightarrow n\pi^0$. At lower energy, the performance of the detector is calibrated using a Cockcroft-Walton accelerating protons up to 1 MeV on a $Li_2B_4O_7$ target to produce photons from nuclear reactions.

In Figure 2.14, a Monte Carlo simulation of the energy response of the LXe calorimeter is shown. The w parameter is the reconstructed conversion depth of the photon in the detector. The fit has been performed with a Crystal Ball function, consisting of a gaussian core and a power-law low-end tail. The width of the gaussian provides a estimator of the energy resolution. It can be noticed that the core is narrower and the low energy tail is smaller in the MEGII than in the MEG calorimeter, this is due to the improved light collection, which allows to reduce the energy leakage.

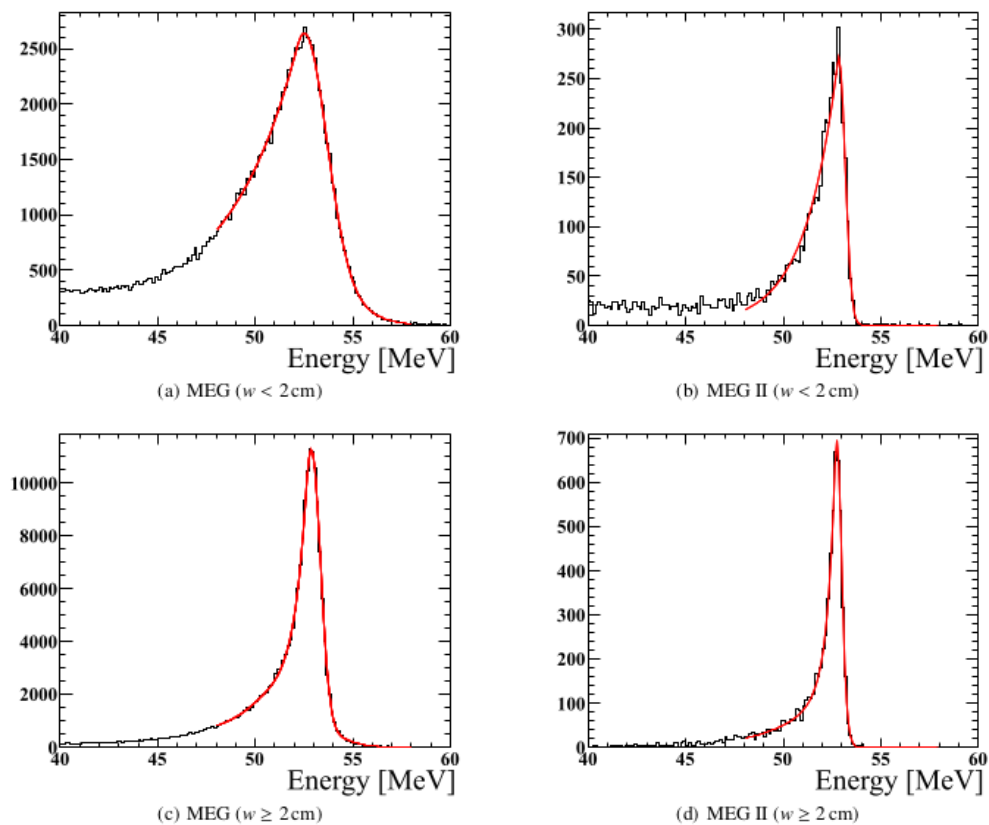


Figure 2.14. Energy PDFs for simulated $E_\gamma = 52.83$ MeV, (a) and (c) for the MEG experiment, (b) and (d) MEGII. The w represents the reconstructed conversion depth.

2.4 COBRA Magnet

The COBRA (COnstant Bending RAdius) magnet is a superconducting magnet, which surrounds all the detectors except for the LXe calorimeter. It has been developed for the MEG experiment with some peculiar characteristics. The COBRA generates an axial graded magnetic field with a cylindrical symmetry along the z -axis. At the center, $z = 0$, the field reaches the maximum intensity of 1.27 T and decreases while increasing $|z|$ down to 0.49 T near to the DCH endcaps. The graded magnetic field is necessary to sweep away the low-energy positrons. COBRA is composed by five coils with three different radii. The central coil's thickness is $0.197X_0$ and in this way, it is possible to minimize the energy loss of the photons before they arrive to the calorimeter. Moreover, there are two gradient coils and two end coils. In Figure 2.15 the different behaviors of a positron in COBRA magnetic field and in uniform magnetic field are compared.

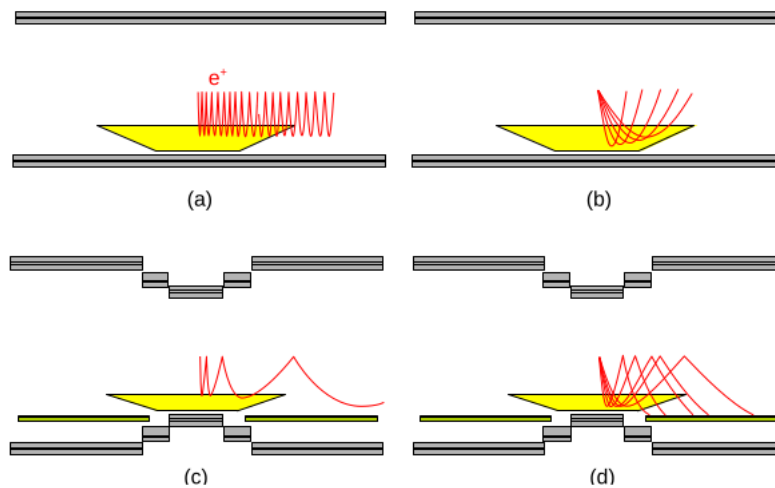


Figure 2.15. Positron tracks in the COBRA magnet field (figure (c) and (d)), compared with those in a uniform magnetic field (figure (a) and (b)). In (a) and (c) the positron is emitted perpendicular to the direction of the beam.

Normal conductive magnets are installed at both sides of COBRA in order to reduce the strength of the magnetic field in the region in which it would affect the calorimeter's PMTs performances. In Figure 2.16 the distribution of the magnetic field intensity around the LXe detector is represented.

2.5 Timing Counter

The timing counter is used to measure the time of flight of the positron from the muon decay. The MEG timing counter was composed by 30 scintillator bars of $80 \times 4 \times 4 \text{ cm}^3$. Each scintillator was read out by fine mesh PMTs at both ends. It presented a good intrinsic time resolution but the operative time resolution was worst because of different causes: PMT degradation performances due to the COBRA

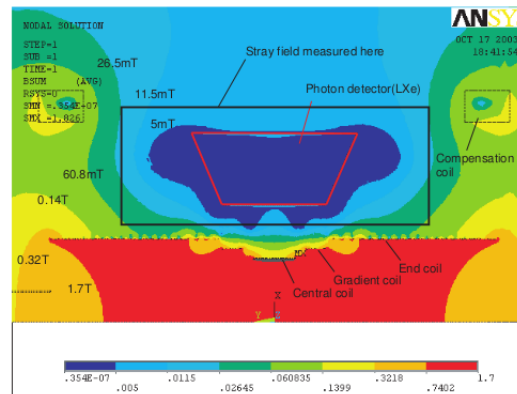


Figure 2.16. Magnetic field intensity distribution around the LXe detector.

magnetic field, timing alignment among the bars and electronic time jitter. For the MEGII experiment, all the TC has been replaced with a new one. The new pixelated Timing Counter (pTC) consists of two sets of semi-cylindrical shape scintillation detectors similar to the MEG timing counter, but each detector is composed by many ultra-fast plastic scintillator tiles coupled to two SiPMs (Silicon PhotoMultipliers). A total of 512 tiles constitute the pTC. Each tile is $90 \times 40 \times 5 \text{ mm}^3$ as in Figure 2.17 where a single tile with their support is shown.

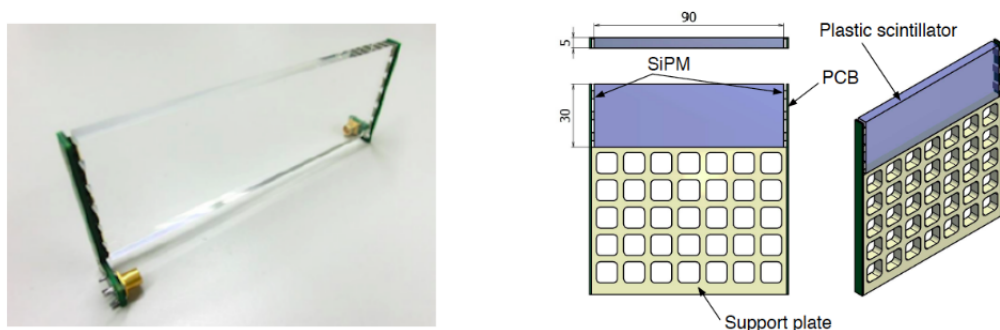


Figure 2.17. On the left side a pTC tile is shown, on the right side a schematic of the support plate with the SiPM read-out can be seen.

The two semi-cylindrical modules are placed upstream and downstream of the target in the COBRA. The 256 counters per module occupy the space between the drift chamber and the COBRA magnet (Figure 2.18). There are 16 aligned counters spaced at 5.5 cm and placed at 45° with the beam direction, in order to have the signal positron trajectories perpendicular to the single counters. The pTC covers $23.0 < |z| < 116.7 \text{ cm}$ along the beam axis and the angular coverage of $-165.8^\circ < \phi < 5.2^\circ$ guarantees the angular acceptance of the positron when the photons goes to the LXe detector.

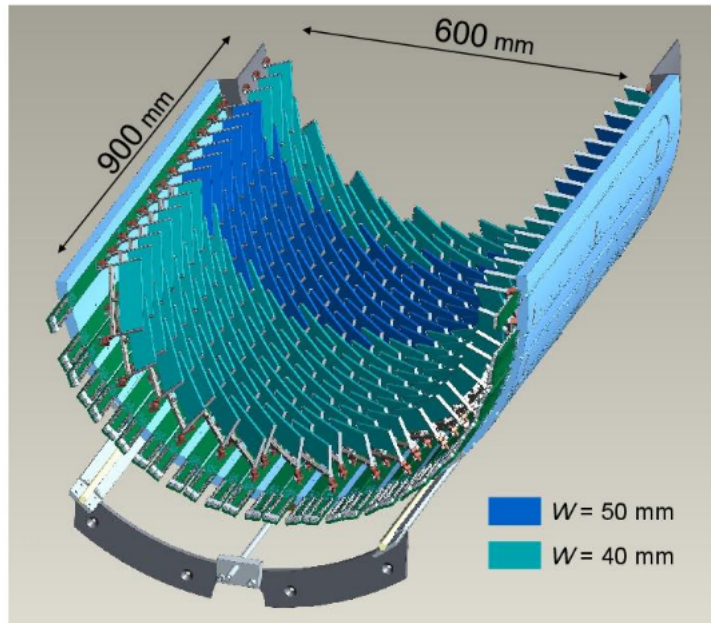


Figure 2.18. Picture of one of the pTC module.

Using a Monte Carlo simulation, the final detector configuration has been simulated to obtain the hit distribution and hit rates in pTC. Figure 2.19 represents a positron from a signal event with its hit pattern in the pixelated timing counter. Every single unit counter has been tested using electrons from ^{90}Sr source and the whole detector has been tested in the engineering runs in 2016 and 2017 using a muon beam. After applying the whole reconstruction analysis, the time resolution of the TC has been estimated to reach the value of ~ 40 ps improving by a factor of 2 that obtained in the MEG timing counter (76 ps). In Figure 2.20 the resolution as a function of the number hits is shown.

2.6 Radiative Decay Counter

The Radiative Decay Counter (RDC) is a completely new detector, which was not present in the MEG experiment. This detector allows to reduce the accidental background that is the dominant background in MEGII. As explained in subsection 2.1.2, the photons of accidental background can be produced by RMD or AIF. The photons from AIF are reduced by the use of the new drift chamber (see Section 2.7) which has lower mass compared to the MEG drift chamber system. On the other hand, the RMD remains unaltered. For this reason, in order to improve the rejection of the accidental background, it has been decided to introduce a Radiative Decay Counter. The RMDs with high energy photon produce a low energy positron, which essentially performs a helical trajectory around the magnetic field axis. This kind of low energy positrons are not detected by the pTC or the drift chamber but the high energy photons interact in the LXe detector. The RDC is settled downstream of the new cylindrical drift chamber with the purpose to detect the low energy positrons

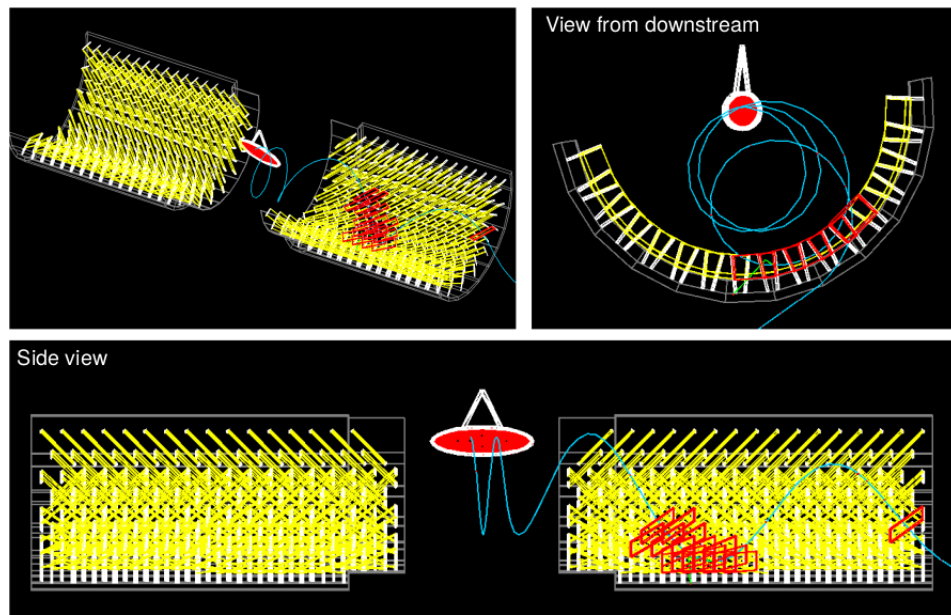


Figure 2.19. Hit pattern in the pTC of a positron from simulated $\mu^+ \rightarrow e^+\gamma$.

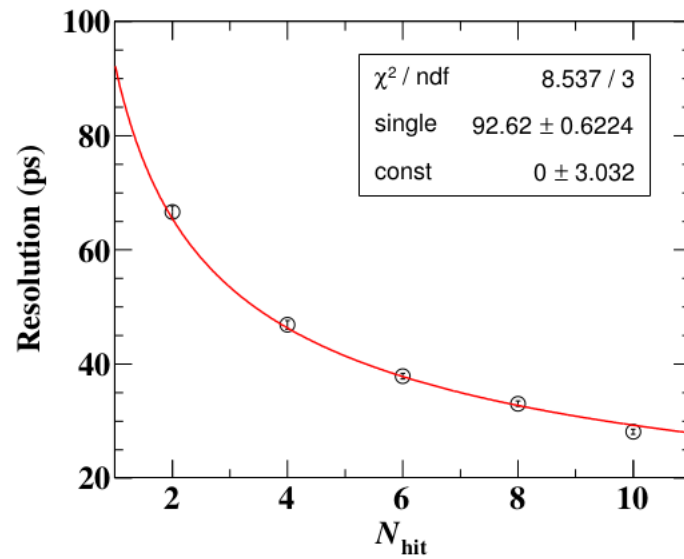


Figure 2.20. Time resolution as a function of number of hits measured in the pTC in the pilot run during 2016. The red line is the best fit function.

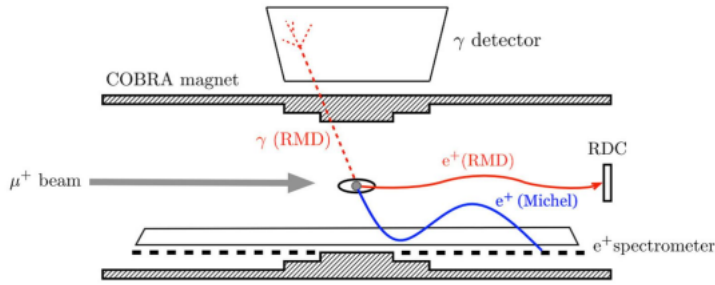


Figure 2.21. Schematic of the low energy positron detected by the new RDC.

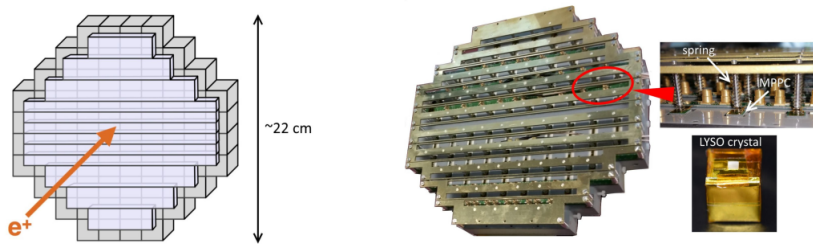


Figure 2.22. Schematic view of the RDC on the left figure. On the right figure the LYSO crystals are shown.

from RMD. According to the simulation, the RDC can detect $\sim 42\%$ of the RMD photon background with the gamma energy $E_\gamma > 48 \text{ MeV}$. In Figure 2.21 there is an example of low energy positron detected by the RDC.

The detector is composed by 12 plastic scintillator bars which measure the time of the positrons, while 76 LYSO crystals behind constitute the calorimeter for the energy measurement. Since the background rate is larger close to the beam axis, the width of the plastic scintillators in the central region is 1 cm while it is 2 cm in the outer part. The size of each LYSO crystal is $2 \times 2 \times 2 \text{ cm}^3$. In Figure 2.22 a schematic view of the RDC is shown.

The use of this new detector will improve the MEGII sensitivity by 15% according to the simulations. All the performances of the RDC are summarized in Figure 2.23.

Parameter	Value
LYSO energy threshold	30 keV
RMD detection efficiency	100%
LYSO energy resolution	8%
Time resolution	100 ps
Accidental probability	9%
RMD acceptance	88%

Figure 2.23. RDC expected performances. The accidental probability is the probability of observing Michel positrons.

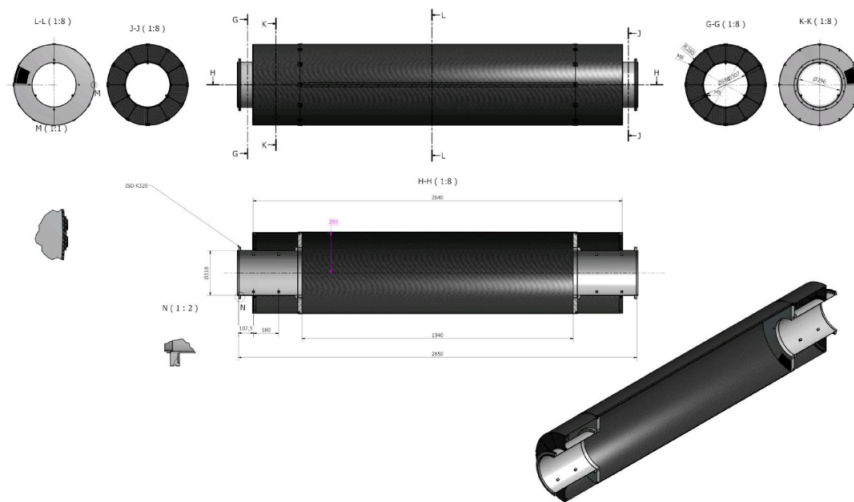


Figure 2.24. MEGII drift chamber structure.

2.7 Cylindrical Drift Chamber

The cylindrical Drift Chamber (DCH) constitutes the positron spectrometer of the MEGII Experiment. The MEGII DCH is used to measure the positron energy, the positron production angle, the production vertex in the target and together with the timing counter, the positron time of flight. In the previous MEG Experiment, the drift chamber system was made by 16 drift chamber modules spaced by 10.6° intervals and each module was filled with a mixture of helium-ethane 50 : 50. The modules were trapezoids with base lengths of 40 *cm* and 104 *cm* respectively. Thanks to its low-mass the average amount of material seen by a positron was $\sim 2 \cdot 10^{-3} X_0$. This system has been completely replaced with a new one. The MEGII DCH is a unique volume low-mass detector with a high granularity and a stereo wires configuration. It is placed around the beam and inside the COBRA magnet. This detector has a cylindrical symmetry along the beam axis (z axis), covers all the azimuthal angle ϕ and it is divided into 12 identical sectors.

The mechanical structure, shown in Figure 2.24, is a 1.91 *m* long cylinder, inner radius of 170 *mm* and outer radius of 290 *mm*. The wires are not parallel to the chamber axis, which is coincident with the beam axis. Indeed, the wires form with the z -direction a stereo angle that varies from 6° degrees in the innermost layer to 8.5° degrees in the outermost one. This is used to measure the z coordinate of the reconstructed hits along the beam axis combining the information of adjacent planes.

The total number of wires is 13056 for an equivalent radiation length of $1.58 \cdot 10^{-3} X_0$. The elementary unit of the drift chamber is a square shape drift cell. The single drift cell dimensions vary: in the innermost layer the side is 6.6 *mm* and in the outermost layer is 9.0 *mm*. Each drift cell consists of eight cathode field wires which surround the central anode sense wire. The anode sense wires are gold-plated tungsten wires of 20 μm diameter and are set at a positive voltage ($\sim 1500 - 1600$ *V*) in order to generate the electric field in which the ionization electrons drift and are amplified. In Figure 2.25 a simulation of the drift lines taking into account the effect of the

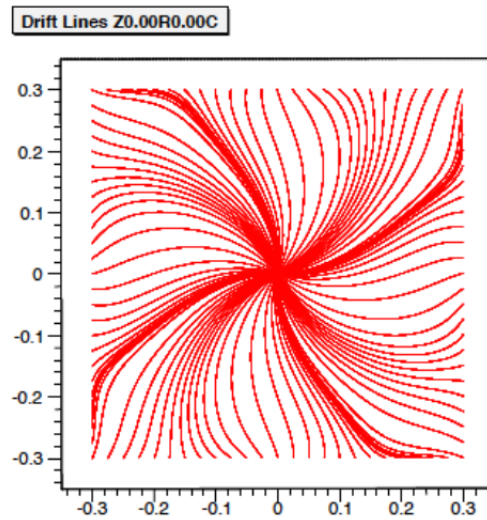


Figure 2.25. Simulated drift lines in presence of COBRA magnetic field.

COBRA magnetic field is shown. The signal from the anode sense wires is read-out at both the ends with the front-end electronics which are custom high-bandwidth pre-amplifiers. The cathode field wires are silver-plated aluminum wires of $40 - 50 \mu\text{m}$ diameter connected to the ground. The configuration of the drift cells at the center of the DCH is reported in Figure 2.26. A number of 192 drift cells constitutes each layer. The active volume of the DCH is composed by 10 layers and is closed by a plane of guard wires set to a lower voltage than the anodes. The guard wires are silver-plated aluminum wires of $50 \mu\text{m}$ diameter and are needed to reduce and close the electric field lines near the edge of the active volume. The chamber with all the wires is shown in Figure 2.27.

The DCH at both ends is closed by two 30 mm thick gold-plated aluminum wheels with twelve radial spokes. On both the internal faces of the end plates there are four perforated pipes which allow the flushing of the gas inside the drift chamber. The total volume is about 380 liters of gas. The gas used to fill the drift chamber is a mixture helium-isobutane. The helium has been chosen because of its properties, in particular the large radiation length, $X_0 \sim 5300 \text{ m}$ at standard temperature and pressure, implies a small contribution to the multiple scattering of the positron. Moreover, it is required a quantity of 10 – 15% of isobutane in order to avoid self-sustained discharges. The average number of ionization clusters created in the gas volume for $\text{He} : i - \text{C}_4\text{H}_{10} \text{ } 90 : 10$ is $\sim 12 \text{ cm}^{-1}$. While the drift velocity in the same mixture is $\sim 3 \frac{\text{cm}}{\mu\text{s}}$. Preliminary tests have been done on prototypes in a cosmic-ray facility and a test beam has been performed [20] showing an expected spatial resolution of $\sim 100 \mu\text{m}$. The MEGII drift chamber expected resolutions are:

$$\sigma_{p_{e^+}} = 130 \text{ keV}, \quad \sigma_{\theta_{e^+}} = 5.3 \text{ mrad}, \quad \sigma_{\Phi_{e^+}} = 3.7 \text{ mrad} \quad (2.6)$$

The expected tracking efficiency is 78%, while the matching efficiency of the drift chamber with the timing counter reaches 90%.

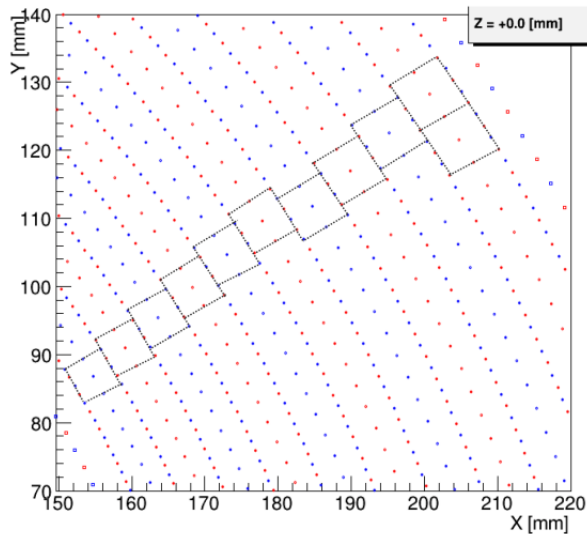


Figure 2.26. Drift cells configuration at the center of the drift chamber.

2.8 DAQ System

In the previous MEG experiment, the data acquisition was based on a fast waveform digitization developed at PSI, called Domino Ring Sampler (DRS). In MEGII, the total number of the channels is much bigger than in MEG. This is due to the higher granularity of the upgraded detectors. To deal with the increased number of the channels (more than 9000 channels in MEGII against the approximately 3000 in MEG), the electronics is redesigned. The new electronics has been chosen with the purpose to digitize the whole waveform. The trigger and the DAQ system of MEGII have been integrated into the same board called WaveDREAM developed at PSI. The WaveDREAM board (WDB) integrates the digitization, the basic trigger, DAQ functionalities, high voltage and amplification. The WDB contains an amplifier and a waveform shaper, a bias voltage supply for the SiPM and two Domino Ring Sampler (DRS4) chips for the waveform digitization, which are connected to two ADCs. The outputs of the ADCs are transmitted to a Field-Programmable Gate Array (FPGA), which treats trigger algorithms. The entire front-end electronics has been optimized to give an overall bandwidth of about 1 GHz. There are two gain stages, which can be combined to increase the signal amplitude from the sense wires and the SiPM.

Figure 2.28 shows a picture of a WaveDREAM board. The trigger system uses the comparators implemented in each input channel of TC and LXe for the determination of the relative time of positron and photon. Moreover, the photon energy and direction are estimated for trigger purposes. The MEGII trigger rate is expected to be ~ 10 Hz comparable with those reached in MEG.

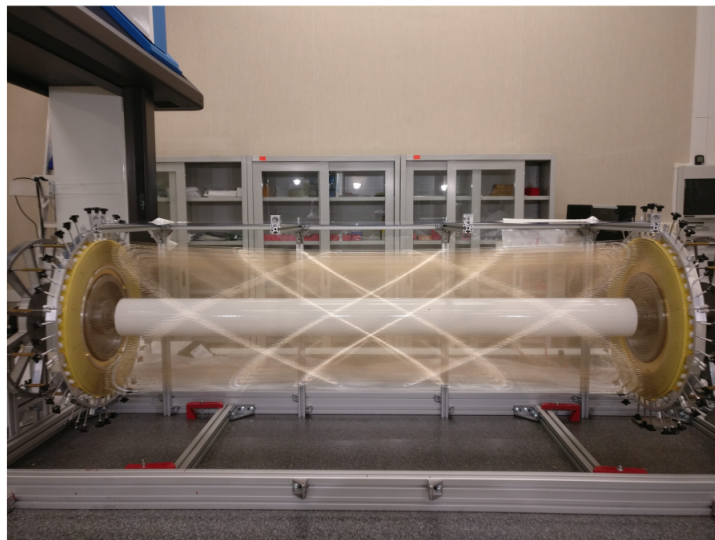


Figure 2.27. A picture of the MEGII drift chamber after the wiring process.



Figure 2.28. A picture of the WaveDREAM board.

2.9 MEGII expected performances

In Table 2.1 all the expected performances of MEGII are reported. The resolutions of the upgraded detectors are compared to those reached in MEG.

Parameter	MEG	MEGII expected
$\sigma(E_e)$	306 <i>keV</i>	130 <i>keV</i>
$\sigma(\theta_e)$	9.4 mrad	5.3 mrad
$\sigma(\Phi_e)$	8.7 mrad	3.7 mrad
$\sigma(z)$	2.4 mm	1.6 mm
$\sigma(y)$	1.2 mm	0.7 mm
$\sigma(E_\gamma)$	2.4% ~ 1.7%	1.1% ~ 1.0%
$\sigma(G_{\parallel})$	6 mm	5 mm
$\sigma(G_{\perp})$	5 mm	2.6 mm
$\sigma(t_{e\gamma})$	122 <i>ps</i>	84 <i>ps</i>
$\epsilon(\gamma)$	63%	69%
$\epsilon(e)$	30%	70%

Table 2.1. MEG and MEGII resolutions and efficiencies are shown.

The variables (z, y) are the vertex coordinates, $G_{\parallel, \perp}$ determine the conversion photon position and ϵ represents the efficiencies.

Chapter 3

Event Reconstruction

In this chapter, the strategies and the algorithms for the event reconstruction are explained. A particular attention is dedicated to the DCH hit reconstruction, which is described in more details.

3.1 Positron Reconstruction

The four quantities associated with the positron and measured by the detectors are the energy, time of production, the angles and the vertex at the target. In particular, the positron momentum is measured through the drift chamber, while the positron time is measured using both the drift chamber and the timing counter. Since these two are completely new detectors, the analysis has to be different from that used in MEG.

Starting from the time of flight of the positron, it is possible to determine the positron production time in the target. The first step is to reconstruct the hits of each event in both detectors using a waveform analysis. The hits found in the drift chamber found are used to reconstruct the positron track. Meanwhile, a clusters analysis is performed to reconstruct the track in the timing counter. The two tracks found respectively in the DCH and in the pTC are then matched. In this way, the positron time t_e is calculated considering the informations from both DCH and pTC, and it results:

$$t_e = \frac{\sum_i^n (t_i^{TC} - l_i/c)}{n} - L_{DCH}/c \quad (3.1)$$

where i runs over the hits in the TC, l_i is the path length from the first hit counter in TC to the i -th hit counter, t_i^{TC} is the time measured by the i -th hit counter and L_{DCH} is the path length from positron vertex to the first hit in the TC reconstructed by DCH.

Starting from the matched track in the DCH and TC, the entire positron trajectory is then fitted considering the dynamic of a charge particle moving into a magnetic field taking in account also the crossed materials. The track is extended up to the positron emission point in the target, where the momentum, the vertex and the angles of the positron at the target are determined.

3.1.1 DCH Waveform analysis

In the DCH the algorithm developed to search for the signal uses the sum of the waveforms which are read-out at the ends of one wire. The waveforms are digitized at a sampling speed of 800 MHz in a 1280 ns window by the WaveDREAM. An example of a waveform from a sense wire for a simulated signal positron is shown in Figure 3.1. The trigger timing is such that the time window is centered around the signal of a hit. The different ionization clusters can be observed.

The waveform analysis procedure is the following:

- in the region before the signal, the baseline (mean and RMS) is calculated, if a pile-up hit is found in that region the expected value of 0 for the mean and 2 mV for the RMS are set
- a hit is found if the waveform goes above a pre-defined threshold (5 RMS over the baseline)
- others hits are searched after the waveform stays at least consecutively 5 ns below the threshold or at maximum after 250 ns which is the maximum expected hit duration

The algorithm uses a constant threshold method combined with a linear interpolation to compute the hit time. In particular, the algorithm fixes a threshold equal to the sum of the baseline and three times the value of RMS previously calculated. A linear interpolation is then performed between the first bin above the threshold with the bin before it. The time of the point of intersection of the linear interpolation with the constant threshold is assumed as the hit time. For the determination of time associated with a hit, the waveforms from the two different ends of the wire are used. The final hit time reconstructed t_{hit} is computed performing a constant threshold method in both the waveforms:

$$t_{hit} = \frac{t_{hit,u} + t_{hit,d}}{2} - \frac{L}{2v} \quad (3.2)$$

where $t_{hit,u}$ is the hit time calculated at the upstream end of the wire and $t_{hit,d}$ is the hit time calculated at the downstream end of the same wire, L is the wire length and v is the signal propagation velocity. The $t_{hit,u}$ and $t_{hit,d}$ variables contain a calibration constant depending on the read-out chain which need to be determined. More details of this formula are presented in Section 4.

On the other hand, the charge is determined by integrating the sum of waveforms in the hit region. Moreover, starting from the charge asymmetry at the two ends it is possible to determine the position of the hit along the z direction:

$$z = A \times L_{eff} \quad (3.3)$$

where A is the charge asymmetry and L_{eff} is the effective length of the wire (see Section 5). The waveform analysis needs to take into account the pile-up i.e. hits coming from the overlapping positrons in the acquisition window. The presence of the pile-up affects the hit reconstruction generating wrong reconstructions of the signal and inefficiencies in the reconstruction, but the algorithms have been optimized to reduce these effects.

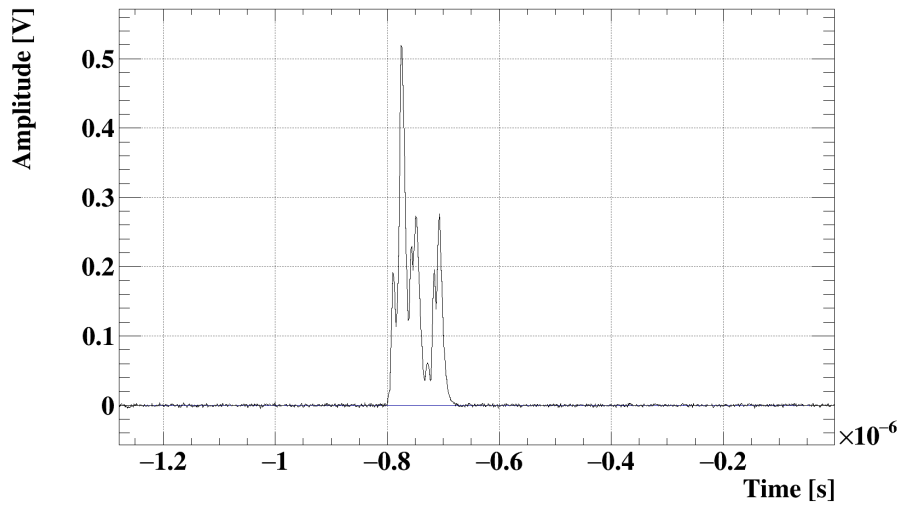


Figure 3.1. An example of a waveform from a DCH sense wire from a simulated signal positron.

The pile-up contribution can be evaluated as follow:

$$N_p = I \times \Delta t \times \alpha \quad (3.4)$$

where N_p is the number of pile-up events, I is the intensity of the MEGII muons beam, Δt is the time window and α is the geometric acceptance. A high fraction of the waveforms are affected by at least one pile-up event. In Figure 3.2 a waveform with a hit of signal more a pile-up hit is shown.

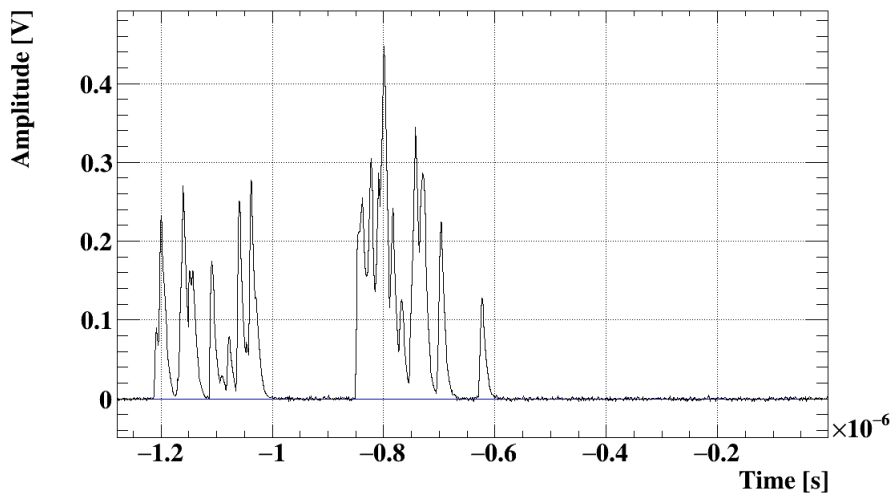


Figure 3.2. A simulated waveform from a DCH sense wire from a signal positron more pile-up. The pile-up hit is clearly shown and precedes the hit of signal.

3.2 Photon Reconstruction

A photon with an energy of $\sim 52 \text{ MeV}$, interacts with LXe especially via pair production process producing an electromagnetic shower. The position, the energy and the timing of the photons are reconstructed from the waveforms from each PMT and MPPC digitized by the WaveDREAM board. The main uncertainty in the reconstruction process derives from the event-by-event fluctuations in the shower development.

Inside the LXe calorimeter, a special coordinate system (u, v, w) is used in the photon reconstruction: u coincides with the z -axis along the beam direction, v is directed along the negative ϕ -direction at the radius of the inner face, and w is the reconstructed conversion depth.

3.2.1 Waveform analysis

The reconstruction starts with a waveform analysis that extracts charge and time for each PMT and MPPC waveform. Algorithms have been developed to identify and eliminate events with two overlapping photons (pile-up). In order to maximize the signal-to-noise ratio for the charge determination, a digital high-pass filter is applied to the raw waveforms. The time is determined as the time when the pulse reaches a defined fraction (20%) of the maximum pulse height. The charge is computed by integrating the filtered pulse and the number of photo electrons, $N_{pe,i}$ detected by the i -th detector is:

$$N_{pe,i} = Q_i / (e \cdot G_i(t)) \quad (3.5)$$

where Q_i is the charge measured and G_i is the gain of the i -th PMT or MPPC. Then, it is possible to compute the total number of scintillation photons:

$$N_{npho,i} = N_{pe,i} / (\epsilon_i(t)) \quad (3.6)$$

where ϵ_i is the product of the quantum efficiency with the collection efficiency of the i -th PMT or MPPC. The gain and the efficiency are continuously monitored and calibrated using LED and α sources respectively, positioned inside the detector.

3.2.2 Photon position reconstruction

The position of the photon interaction vertex is determined by minimizing a χ^2 -function:

$$\chi_{position}^2 = \sum_i^{PMT/MPPC} \frac{N_{pho,i} - c \times \Omega_i(u, v, w)}{\sigma_{pho,i}(N_{pho,i})} \quad (3.7)$$

where c is a free parameter, Ω_i is the solid angle subtended by the photon detector and $\sigma_{pho,i}(N_{pho,i})$ is the uncertainty of the number of photons detected from the i -th PMT or MPPC. The χ^2 function is minimized with respect to the photon conversion coordinates (u, v, w) . The initial estimate of the position is calculated as the amplitude weighted mean position around the photon counter with the maximum signal. To reduce the effect of the shower fluctuations, only detectors inside a radius of 3.5 times the counter spacing are used in the fit for the initial estimate of the position of the interaction vertex.

3.2.3 Photon timing reconstruction

After the reconstruction of the photon interaction vertex in the calorimeter, the time of the first interaction vertex is calculated from each photon counter time, $t_{hit,i}$. The photon conversion time t_γ^c in the LXe is obtained by minimizing:

$$\chi_{time}^2 = \sum_i^{PMT/MPPC} \frac{t_{hit,i} - t_\gamma^c}{\sigma_{t,i}(N_{pe})^2} \quad (3.8)$$

where $\sigma_{t,i}(N_{pe})$ is the time resolution of each photon counter which depends on the number of the photoelectrons. Starting from the time of the first interaction of the photon, it is possible to calculate the photon production time in the target. In fact, knowing that the photon follows a linear path from its production point in the target to the conversion point in the calorimeter, its production time t_γ results to be

$$t_\gamma = t_\gamma^c + l/c \quad (3.9)$$

where l is the linear path from the reconstructed positron vertex to the calorimeter.

3.2.4 Photon energy reconstruction

The photon energy reconstruction is based on the sum of the scintillation photons collected by all PMTs and MPPCs. The energy is obtained by the equation:

$$E_\gamma = F(u, v, w) \times S(u, v, w) \times T(t) \times C \times \sum_i (N_{pho,i} \times W_i) \quad (3.10)$$

where $F(u, v, w)$ is a non uniformity correction factor, $S(u, v, w)$ is a solid angle correction factor, $T(t)$ is a correction factor relative to the light yield changing in time, C is a conversion factor to convert from the number of photons to the energy, W_i is a constant weight. These factors are determined from data or simulations.

Chapter 4

Drift Chamber Time Calibration

The drift chamber is composed of 1920 sense wires, which generate the electric field and collect the signal from the drifting electrons. Due to the geometric acceptance of the TC, the four upper sectors of the DCH are not instrumented and the signal is read-out only from 1280 sense wires. The signal is transmitted to the two ends of each sense wire where is pre-amplified and read-out by the WaveDREAM board. The whole read-out chain needs a time calibration in order to equalizer the response of the various electronics channels. In fact, a time offset can be present between the two different electronic lines of the same wire and between the wires.

In Figure 4.1 a schematic representation of a hit on a wire of the DCH is shown:

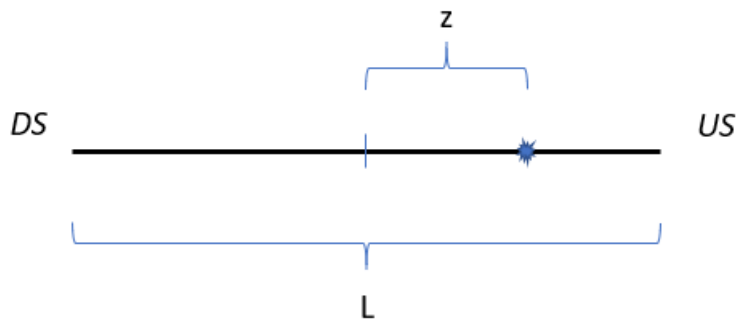


Figure 4.1. Schematic representation of a hit on a wire of the DCH. DS and US are respectively the downstream and upstream read-out channel.

L is the wire length, z is the hit coordinate along the wire, DS represents the downstream read-out channel and US is the upstream read-out channel. The hit time for calibrated detector can be calculated as:

$$t_{hit}^u = t_{hit} + \frac{L/2 - z}{v} \quad (4.1)$$

$$t_{hit}^d = t_{hit} + \frac{L/2 + z}{v} \quad (4.2)$$

where v is the signal propagation speed. Solving for t_{hit} :

$$\frac{t_{hit}^u + t_{hit}^d}{2} = t_{hit} + \frac{L/2 - z}{v} + \frac{L/2 + z}{v} \quad (4.3)$$

thus:

$$t_{hit} = \frac{t_{hit}^u + t_{hit}^d}{2} - \frac{L}{2v} \quad (4.4)$$

Taking into account the calibration constants, the two variables t_{hit}^u, t_{hit}^d are

$$t_{hit}^u = t_{raw}^u + c_1 \quad , \quad t_{hit}^d = t_{raw}^d + c_2 \quad (4.5)$$

where t_{raw} represents the true hit time read at each wire end, c_1, c_2 are the calibration constants to be determined.

In the first part of this chapter, the two different algorithms studied for the determination of the time calibration constants are explained. In the second part, the results of each method on Monte Carlo simulation are shown and an evaluation of the number of signal events necessary to reach a precision on the calibration constants comparable with the one in MEG (500 ps) is done.

4.1 Time Calibration methods

The purpose of this analysis is to develop and to study an algorithm to determine the calibration constants for each DCH read-out channel. In this section, the Monte Carlo simulation and the two algorithms are presented: a template fit method and a constant fraction method have been considered.

4.1.1 Monte Carlo simulation

The events used in this analysis have been generated using the MEG-II software, which is constituted by:

- *gem4* a Monte Carlo simulation based on the GEANT4 [21] toolkit for the simulation of the passage of particles through matter
- *bartender* the code that allows DAQ electronics simulation and pile-up simulation
- *analyzer* the code for the event reconstruction

The MEG-II software is based on C++ programming language. The output of the whole simulation chain is analyzed using the ROOT package [22].

Figure 4.2 shows an example of the reconstructed hit time distribution from a signal positron of DCH wire (layer 0 DS read-out, 10^4 signal events): the signal positron represents a positron from the $\mu^+ \rightarrow e^+\gamma$ decay, therefore with a 52.8 MeV momentum and crossing most of the detectors. The positron during its trajectory in the DCH crosses the drift cells and the drifting electrons are collected by the sense wire, which transmits the signal at the two ends. The drift time of the electrons in a DCH cell depends on the distance between the positron trajectory and the sense

wire: considering the drift velocity equal to $\sim 3 \text{ cm}/\mu\text{s}$ and an average dimension of the drift cells equal to $\sim 8 \text{ mm}$, the drift time for a track, which hits the border of the cell is expected to be $\sim 190 \text{ ns}$. The distribution of the reconstructed hit time is related to the drift time distribution and its shape is related to the geometry of the drift cells. The peak is due to the trajectories, which cross the cells closest to the position of the sense wires. The end point represents the hits at the border of the drift cells. The distribution time length is related to the width of the DCH cell. In the Monte Carlo production, the rise time in which the reconstructed hit time distribution starts is the same for each read-out channel. In real data, the read-out chain can introduce differences in the rise times, which are the calibration constants to be determined. The distribution in Figure 4.2 is not realistic: the

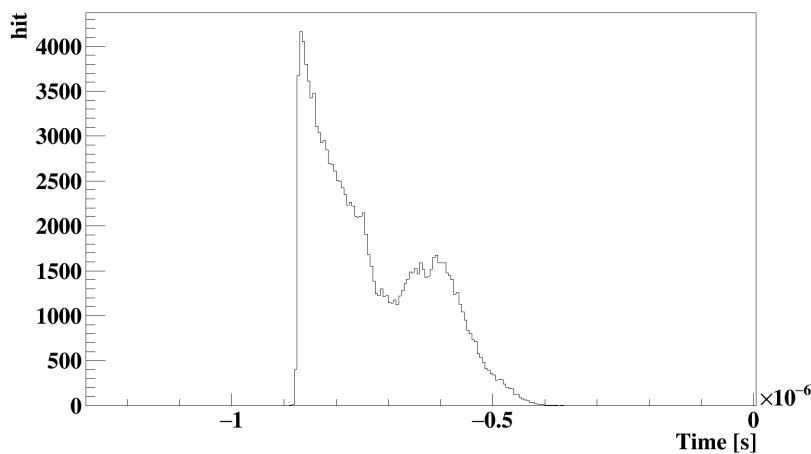


Figure 4.2. Simulated distribution of the DCH reconstructed hit time (all wires, layer 0 DS, 10^4 signal events).

presence of the pile-up hits needs to be considered in the simulation. Figure 4.3 shows the distribution realized by mixing 10^3 signal events with the expected pile-up fraction. The initial peak is due to the pile-up hits accumulated in the end of the previous acquisition time window. Since a large statistic is necessary to evaluate the calibration constants and the simulation of the mixed events is highly time consuming, it has been decided to develop the algorithms using only signal events distributions from full simulated signal events and to include the pile-up, a flat background has been randomly generated in the correct proportion between signal and pile-up. The obtained distribution is shown in Figure 4.4. Several Monte Carlo samples have been generated for a total of $6 \cdot 10^5$ signal events. Two algorithms will be illustrated in the following sections: template fit method and constant fraction method.

The development of the algorithm and the study have been performed in two steps. In the first step, the algorithm stability as a function of the size of the fitted sample has been studied. The sample sizes used for this study are: 10^3 , $5 \cdot 10^3$, 10^4 , $2.5 \cdot 10^4$, $5 \cdot 10^4$ and 10^5 signal events.

In the second step, the fit parameters have been studied separately for each read-out channel. A number of $4 \cdot 10^5$ signal events more have been generated and the total

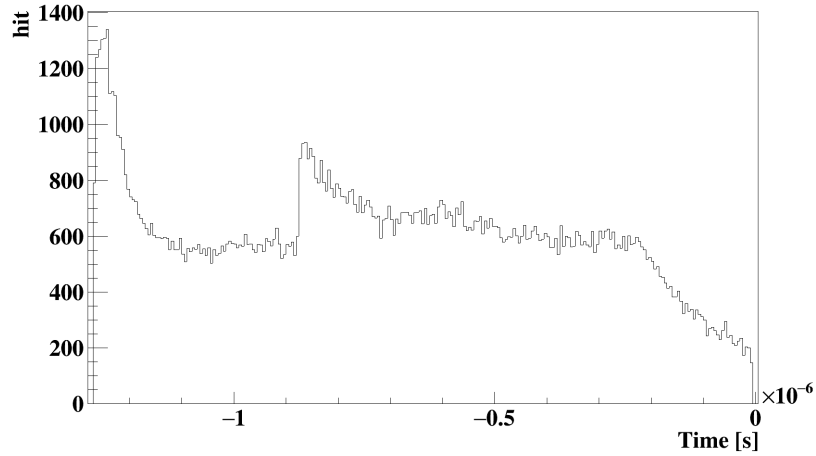


Figure 4.3. Simulated distribution of the DCH reconstructed hit time (all wires, layer 0 DS, 10^3 signal events plus pile-up). The peak presents at low times is due to the pile-up hits accumulated in the previous acquisition window.

sample have been subdivided in: 20 samples of 10^4 signal events, 10 samples of $2.5 \cdot 10^4$ and 10 samples of $5 \cdot 10^4$ signal events.

The constant fraction method has been first studied with 20 samples of 10^4 , 10 samples of $2.5 \cdot 10^4$ and 10 samples of $5 \cdot 10^5$ for a total of $5 \cdot 10^5$ simulated signal events without pile-up hits. Then, it has been tested using 10^3 signal events more pile-up.

4.1.2 Template fit

The template fit method consists in comparing the measured time distribution with a reference distribution called template distribution. The template distribution is an high statistic distribution from Monte Carlo simulation or from data. In this analysis, the template is realized using the Monte Carlo simulated events. The template histogram is superimposed to the measured histogram and two parameters are fitted: a scale factor, which takes into account the different size of the template and events histograms, and a time offset between the two distributions. In fact, the template fit is performed using a χ^2 function:

$$\chi^2 = \sum_i^{nbins} \frac{(A_i - a \times T_{(i-b)})^2}{\sigma_i^2} \quad (4.6)$$

where A_i is the background subtracted content of the i -th bin of the measured event histogram, T_i is the interpolated content of the $i - b$ th bin of the template histogram, σ_i is the error associated with the i -th bin, a is a scale factor and b is the offset parameter. The flat background is evaluated with a linear fit in the region of the histogram without the time distribution. The index i runs over an optimized bin range. The template bin amplitude T_{i-b} is obtained by linear interpolation of

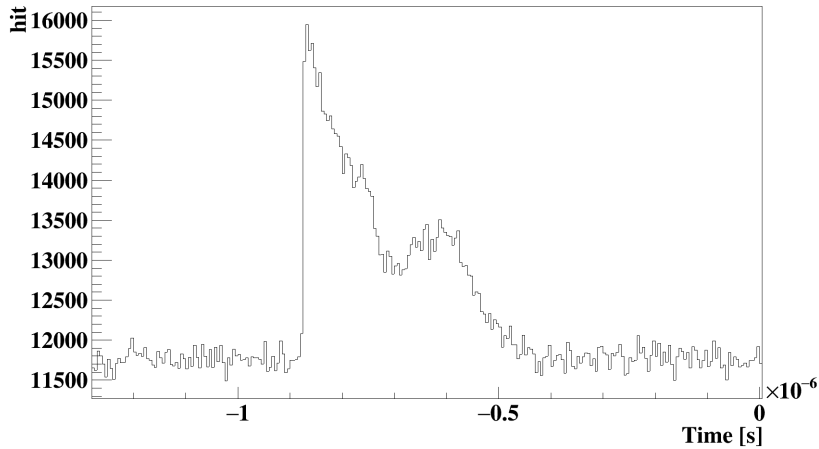


Figure 4.4. Simulated distribution of the DCH reconstructed hit time (all wires, layer 0 DS, 10^4 signal events plus simulated pile-up).

two near bins T_i, T_{i+1} as follow:

$$T(t) = \frac{(T(t_{j+1}) - T(t_j))(t - t_j) + T(t_j)(t_{j+1} - t)}{t_{j+1} - t_j} = T(t_{j+1})\frac{t - t_j}{t_{j+1} - t_j} + T(t_j)\left(1 - \frac{t - t_j}{t_{j+1} - t_j}\right) \quad (4.7)$$

where $j = i - b$ and $T(t_j)$ is the amplitude of the j -th template bin, while $t_j < t < t_{j+1}$ and $T(t)$ is the interpolated bin amplitude.

By minimizing the χ^2 function (4.6) with respect to a and b , the template results to be aligned to the event distribution and a time offset parameter can be determined with its error.

4.1.3 Constant fraction method

The constant fraction method consists in defining a threshold value, which is equal to a fraction of the maximum peak in the reconstructed hit time distribution. The time rise of the distribution is defined as the time of the intersection point between the threshold and the linear interpolation of the first bin above the threshold and its preceding. In Figure 4.5, a reconstructed hit time distribution is shown with a fraction fixed to the 15% of the maximum peak and the linear interpolation is also represented.

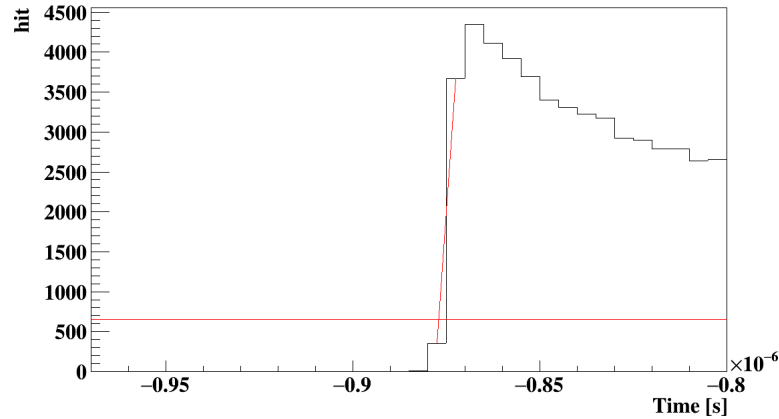


Figure 4.5. An example of the constant threshold method applied to the simulated distribution obtained from the DS read-out of the layer 0.

4.2 Monte Carlo events analysis

The study of the algorithms are reported here and the acquisition time necessary to obtain a precision of 500 *ps* over the calibration constants is calculated.

4.2.1 Template fit Monte Carlo events

A total number of 10^5 signal events have been simulated in order to realize the template histograms. The two steps of the template fit study are reported here with the obtained results.

Template fit stability

For the first part of the analysis, in order to test the stability of the template fit, the following samples has been used: 10^3 , $5 \cdot 10^3$, 10^4 , $2.5 \cdot 10^4$, $5 \cdot 10^4$ and 10^5 signal events. The fit has been performed in the whole range of the hit time distribution i.e. $[-1.28, 0] \cdot 10^{-6}$ s. In the Monte Carlo, all the calibration constants are equally generated for all the ends and all the layers. The parameters are fitted separately for each end putting together the wires of the same layer. In Figure 4.6 the two fitted parameters, the time offset and the scale factor, are reported as a function of the number of the end: the ends from 0 to 9 represent the US end for layer 0-9 and those from 10 to 19 represent the DS end for layer 0-9. In both figures, the black line represents the expected value, which is that used for the Monte Carlo production. The expected value of the offset parameter is 0 *ns*, in fact, in the Monte Carlo simulation all the reconstructed hit time distributions are aligned. The expected scale factor is the ratio of the size of the data and the template samples which is $\sim \frac{10^4}{10^5} = 0.1$. With few exceptions, the fitted values of the scale factor are compatible with the expected value within the errors; this is not the case of the fitted offset. The same features are observed with the samples of $2 \cdot 10^4$ and $5 \cdot 10^4$ simulated signal events (see Appendix A).

In order to test the algorithm also with a time shift different from zero, the template

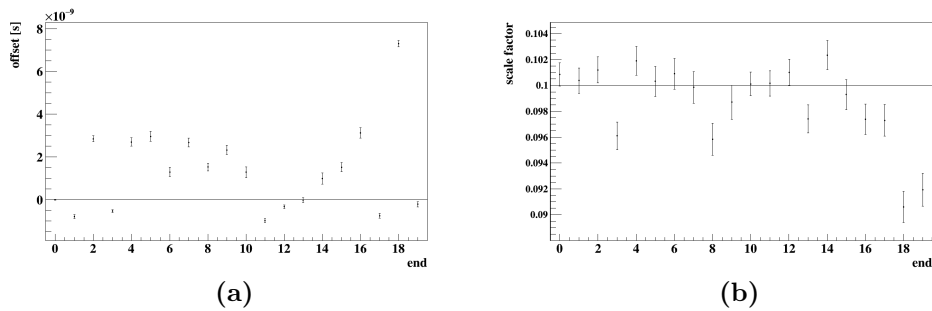


Figure 4.6. Fitted parameters from the template fit method as a function of the end: (a) offset parameter, (b) scale factor. 0-9 are the US read-out of the respective layer and 10-19 represent the DS read-out of the same layer. The black line represents the expected value. The fit has been performed on a sample of 10^4 simulated signal events.

histograms have been shifted by 100 ns. In Figure 4.7 the obtained fit parameters with the same sample size as before are reported. In this case, the scale factors are

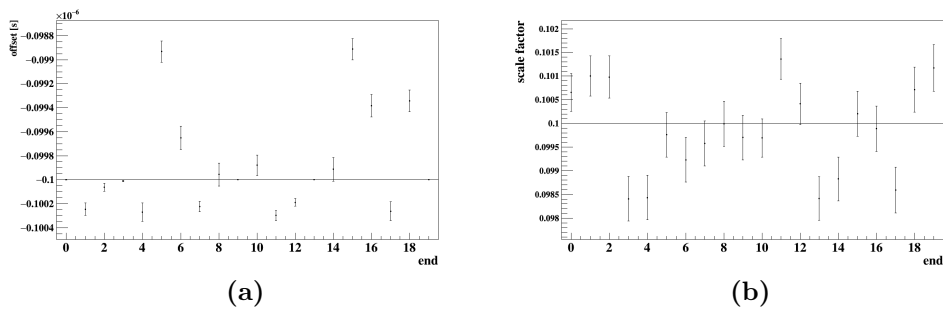
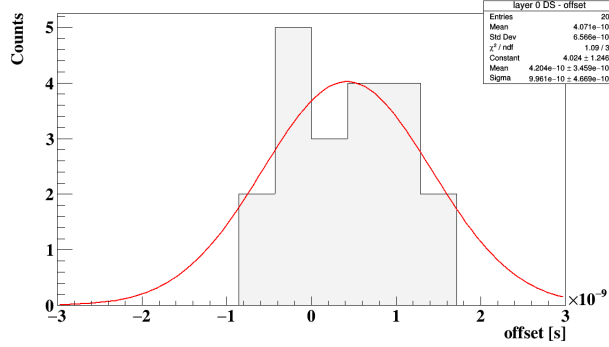


Figure 4.7. Fit parameters as a function of the end for a shifted template: in (a) offset parameters and in (b) the scale factor are reported. 0-9 are the US read-out of the respective layer and 10-19 represent the DS read-out of the same layer. The black line represents the expected value. The fit has been performed on a sample of 10^4 simulated signal events.

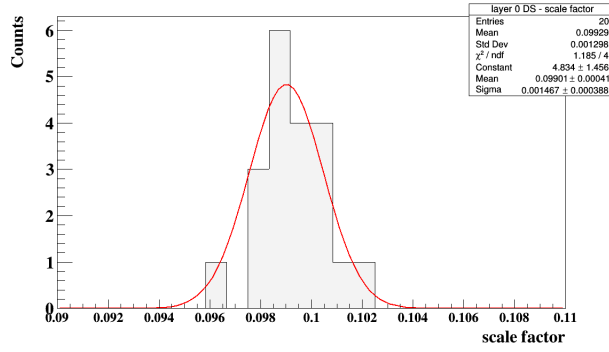
still compatible with the expected value, while the offset parameters are not fitted well. The fitted values obtained in this configuration are shown in Figure 4.7: the offset parameters in (a) and the scale factors in (b) are shown as a function of the end.

Analysis for each end

In order to investigate the fit behavior, several samples for each end are fitted: 20 samples of 10^4 simulated signal events, 10 samples of $2.5 \cdot 10^4$ and $5 \cdot 10^4$ simulated signal events. All the wires of the same layer are regrouped together. The distributions obtained with the samples of 10^4 are here reported. In Figure 4.8 the distributions of the offset parameter in (a) and the scale factor in (b) obtained from the template fit of the layer 0 read-out DS are shown. A more detailed study of



(a)



(b)

Figure 4.8. Layer 0 DS end, fitted parameters (10^4 simulated signal events): offset distribution in figure (a) and scale factor distribution in (b). A gaussian fit has been performed.

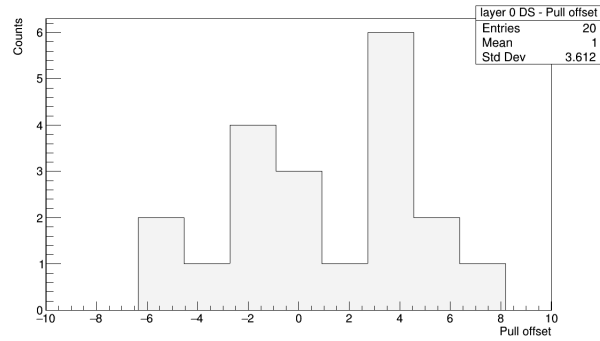
these distributions has been performed realizing the pull distributions defined as

$$pull = \frac{x_{fit} - x_{true}}{\sigma(x_{fit})} \quad (4.8)$$

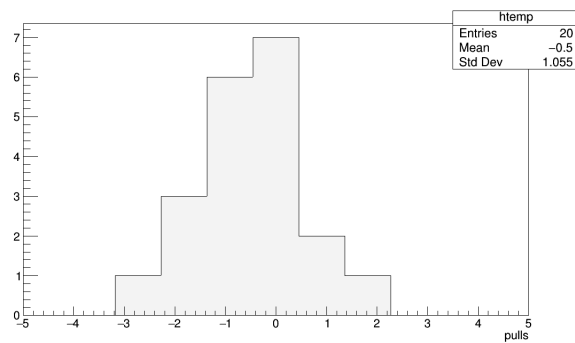
where x_{fit} is the value obtained from the fit, $\sigma(x_{fit})$ its uncertainty and x_{true} is the expected value. In the case of unbiased fit, the expected pull distribution is a gaussian distribution centered in zero with standard deviation equal to one.

In Figure 4.9 the pull distributions of the layer 0 DS are shown. The mean of the pull of the offset parameter is not compatible with zero. This implies the presence of a bias. Moreover, the σ of the pull of the offset parameter is higher than the expected value of one: a miscalculation of the fitted offset error needs to be considered. To better understand this problem a scan of the χ^2 function has been realized showing a large number of local minima. The range of the offset parameter in the fit has then been limited in a time window of $[-50, 50]$ ns minimizing the number of local minima considered in the minimization. Moreover, the fit range has been restricted to $[-0.9, -0.7] \cdot 10^{-6}$ s (Figure 4.10). It has been also increased the uncertainty of each bin:

$$\sigma(i) = f \times \frac{1}{\sqrt{N_i}} \quad (4.9)$$



(a)



(b)

Figure 4.9. Layer 0 DS pull distributions (10^4 signal events): offset distribution in figure (a) and scale factor distribution in (b).

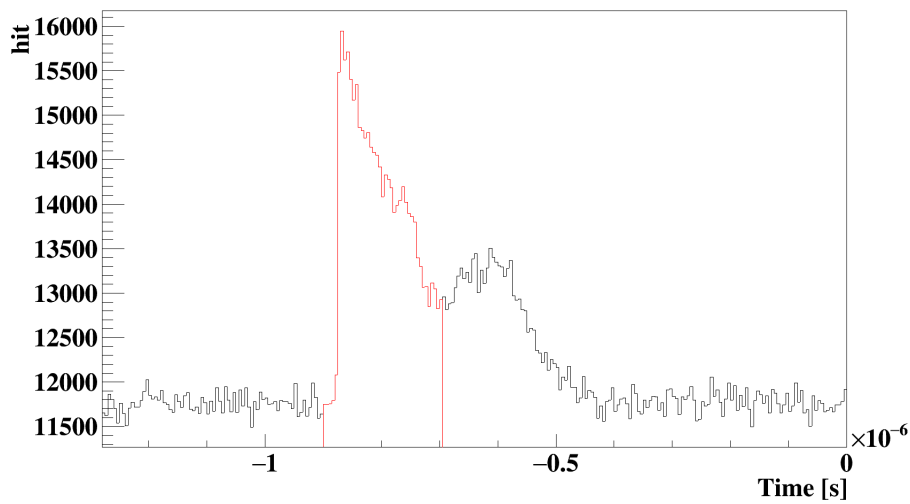


Figure 4.10. Limited range used for the template fit.

where i is the number of the bin and N_i its content. The factor f is chosen as that number which allows to obtain a standard deviation equal to one in the pull of the

offset parameter. In the case of a template fit with a events distribution of 10^4 signal events, the f is equal to 3. The distribution of the offset parameter and scale factor for DS read-out are shown in Appendix B.

All the fitted values for each end are reported in Table 4.1. It results clear that almost all the scale factors are compatible with the expected value of 0.1. Most of the offset parameters are compatible with the expected value of 0 ns. The template fit results instable and an adequate study could be performed to better understand the shape of the χ^2 used in this fit.

Layer DS	offset [ns]	σ_{offset} [ns]	scale factor	σ_{scale}
0	0.31 ± 0.31	0.94 ± 0.39	0.0992 ± 0.0003	0.0013 ± 0.0003
1	-0.26 ± 0.07	0.28 ± 0.08	0.0997 ± 0.0004	0.0014 ± 0.0004
2	0.39 ± 0.16	0.69 ± 0.01	0.0994 ± 0.0003	0.0011 ± 0.0002
3	-0.11 ± 0.09	0.33 ± 0.09	0.0996 ± 0.0003	0.0014 ± 0.0003
4	0.28 ± 0.20	0.83 ± 0.25	0.1000 ± 0.0005	0.0016 ± 0.0004
5	-0.18 ± 0.08	0.30 ± 0.08	0.0998 ± 0.0002	0.0010 ± 0.0003
6	0.54 ± 0.28	0.88 ± 0.29	0.0986 ± 0.0007	0.0021 ± 0.0007
7	-0.06 ± 0.04	0.19 ± 0.03	0.0996 ± 0.0003	0.0013 ± 0.0004
8	0.54 ± 0.28	0.88 ± 0.29	0.0987 ± 0.0004	0.0017 ± 0.0003
9	-0.06 ± 0.04	0.19 ± 0.03	0.0992 ± 0.0004	0.0013 ± 0.0003
Layer US				
0	-0.36 ± 0.20	0.63 ± 0.22	0.0993 ± 0.0007	0.0019 ± 0.0007
1	0.37 ± 0.40	1.72 ± 0.28	0.0978 ± 0.0009	0.0022 ± 0.0011
2	2.23 ± 0.55	2.26 ± 0.39	0.1008 ± 0.0042	0.0063 ± 0.0082
3	-0.28 ± 0.83	1.37 ± 0.94	0.0989 ± 0.0006	0.0015 ± 0.0010
4	0.10 ± 0.32	1.45 ± 0.23	0.0997 ± 0.0004	0.0016 ± 0.0003
5	0.22 ± 0.33	1.47 ± 0.23	0.0997 ± 0.0006	0.0018 ± 0.0008
6	0.30 ± 0.29	0.89 ± 0.42	0.1002 ± 0.0010	0.0024 ± 0.0017
7	0.69 ± 0.97	1.46 ± 1.18	0.1002 ± 0.0004	0.0014 ± 0.0004
8	0.83 ± 0.51	2.22 ± 0.36	0.1009 ± 0.0009	0.0021 ± 0.0015
9	-0.04 ± 0.20	0.87 ± 0.14	0.1001 ± 0.0007	0.0017 ± 0.0009

Table 4.1. Template fit results performed with 20 samples of 10^4 simulated signal events: the mean and the sigma of each fit parameter obtained through a gaussian fit are here reported.

4.2.2 Constant fraction method Monte Carlo events

The constant fraction method has been developed using mainly the 20 samples of 10^4 signal events and then the statistical behaviour of the parameters have been tested with the 10 samples of $2.5 \cdot 10^4$ and $5 \cdot 10^4$ signal events and 10^3 Michel events more pile-up. With this method, the time associated with the intersection point between the threshold and the linear interpolation is studied. This is called edge time.

The first part of this analysis has been performed considering all the ends in the same distribution. The threshold has been varied in the interval $[5;30]\%$ of the maximum peak and then the value has been fixed to 15%. In Figure 4.11, the distributions of the fitted edge time are shown. A gaussian fit is performed to evaluate the mean width of these distributions, which are the variable of interest of this analysis. The obtained χ^2 values are compatible with the expectation. Starting from these distributions, the statistical behavior of the error has been studied. The σ_i of the distribution is expected to vary with the number of the events N :

$$\sigma_i(N) \propto \frac{1}{\sqrt{N}} \quad (4.10)$$

In Figure 4.12 the σ_i of the edge time distribution is reported as a function of the number of events. The red line represents a fit function with two parameters a and b

$$f(N) = \frac{a}{\sqrt{N-b}} \quad (4.11)$$

where N is the number of events. As expected the fit is good as confirmed by the χ^2 value. The analysis has been then focused on the 20 samples with 10^4 . The ten layer has been separated in order to find the width of the distribution of the rise time. In Appendix C all the obtained distributions are reported.

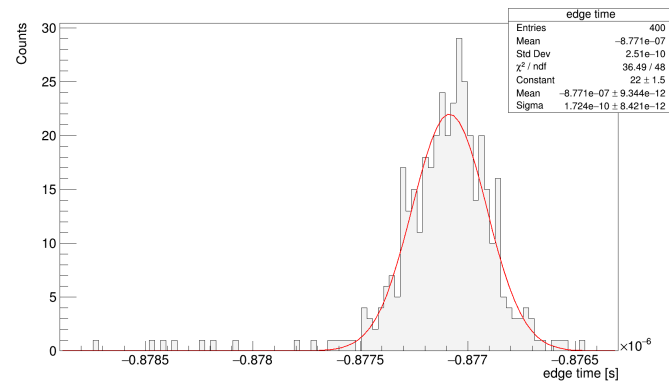
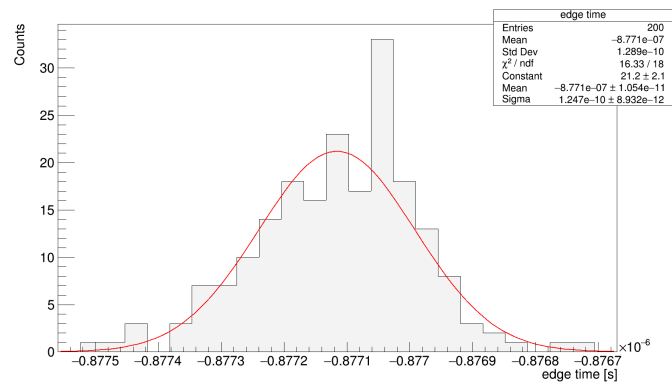
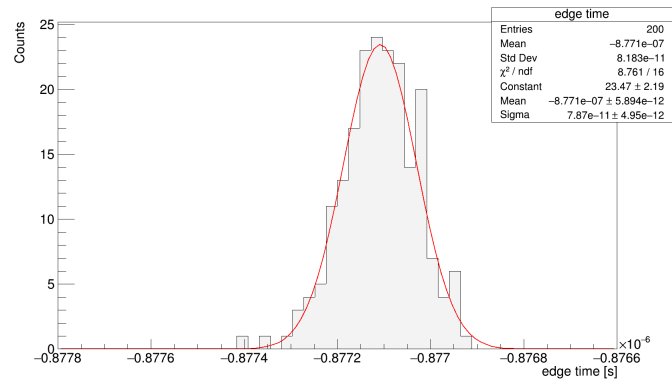
Considering the same time calibration constant for all the wire of the same layer, it is possible to evaluate the number of events necessary to obtain a sensitivity for each wire of 500 ps. To compute the number of events for the calibration is necessary to introduce the occupancy per layer. The histogram of the occupancy is shown in Figure 4.13: the number of hits as a function of the number of the wire is reported. The histogram is realized using one sample of 10^4 signal events. The firsts 192 wires belong to the layer 0 and the lasts 192 to the layer 9. Considering the equation 4.10, it results as follow:

$$\sigma_t(10^4 \text{ events}) = \frac{\sigma_t(N_x)}{\sqrt{10^4/N_x}} \quad (4.12)$$

where $\sigma_t(10^4 \text{ events})$ is the error fit with 10^4 events. The number of events N_x necessary to reach the sensitivity $\sigma_t(N_x) = 500 \text{ ps}$ for each wire is computed:

$$N_x = \left(\frac{\sigma_t(10^4)}{500 \text{ ps}}\right)^2 \cdot 10^4 \quad (4.13)$$

All the results are reported in the Table 4.2. The N_{events} represents the number of events necessary to the calibration of a wire of each layer with at least 100 hits in the sample of 10^4 signal events. Using this approximation, only the boundary

(a) 10^4 signal events(b) $2.5 \cdot 10^4$ signal events(c) $5 \cdot 10^4$ signal events**Figure 4.11.** Distribution of the edge time with 10^4 , $2.5 \cdot 10^4$ and $5 \cdot 10^4$ signal events.

wires for each layer are not calibrated. The acquisition time has been evaluated considering the MEG trigger rate of 10 Hz.

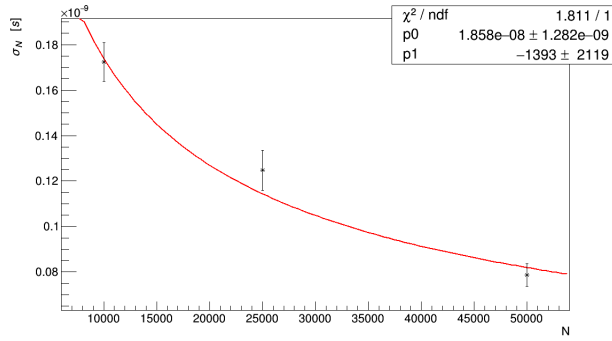


Figure 4.12. The width of the edge time distribution as a function of the number of events.

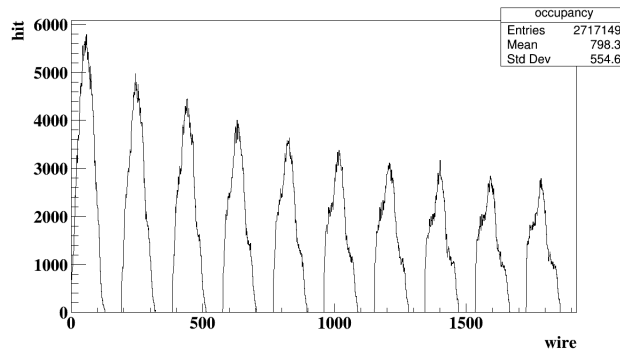


Figure 4.13. Occupancy histogram obtained with a sample of 10^4 signal events.

layer	$\sigma_t(10^4 \text{ events})$ [ps]	N_{events}	DAQ Time [h]
0	146.2	3472158	96
1	103.7	147084	41
2	212.8	5705691	158
3	192.8	414589	115
4	258.2	699150	194
5	190.5	350078	97
6	157.4	228978	63
7	158.8	218971	61
8	213.1	379514	105
9	223.8	403821	112

Table 4.2. Results for each layer with samples of 10^4 signal events.

Pile-up events analysis

A test of the constant fraction method has been performed using 10^3 signal events with simulated pile-up. Figure 4.14 shows the histogram of the signal events more

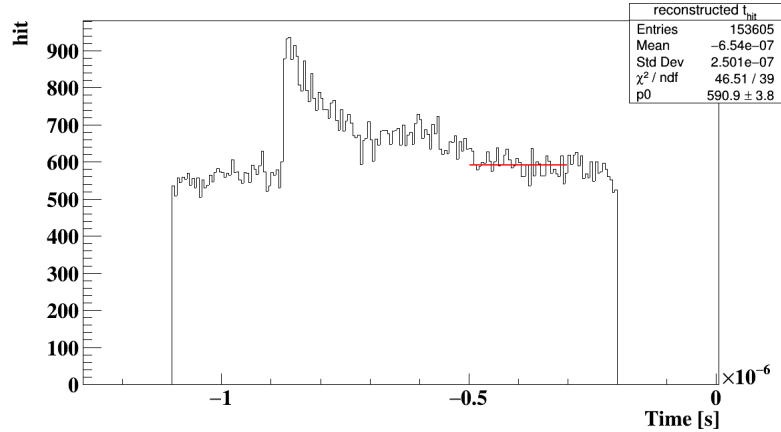


Figure 4.14. 10^3 signal events mixed with $16 \cdot 10^3$ events. The red line represents a fit to estimate the background for the threshold calculation.

pile-up: the initial peak due to the pile-up hits accumulated in the end of the previous window acquisition has been cut in order to optimize the search of the peak of the signal distribution. A fit with a polynomial function has been performed in order to evaluate the background due to the pile-up. The initial peak due to the pile-up hits has been cut in order to optimize the constant fraction method. Different thresholds have been tested with the pile-up events and a 30% of the maximum peak threshold has been used. The distribution of the edge time for all the read-out together is shown in Figure 4.15. The width of the distribution results compatible with the previous study of the error with only signal events. A larger number of samples should be produced in order to separate the different read-out.

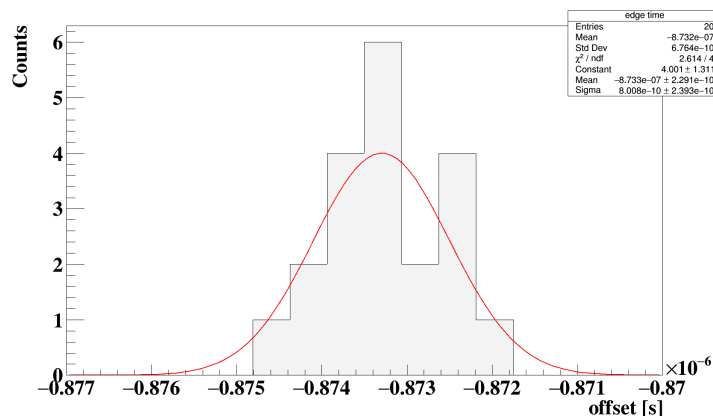


Figure 4.15. Edge time distribution of 10^3 signal events with pile-up for the all the read-out.

Chapter 5

Drift Chamber z Calibration

The z coordinate along the wire can be measured in two different ways: through the time difference at the two ends of a wire and with a charge division method. The z calculation with the time difference method is:

$$z = \frac{(t_{up} - t_{down})}{2} \cdot v \quad (5.1)$$

where t_{up} is the upstream end time and t_{down} is the downstream end time, while v is the signal propagation speed. This method is automatically calibrated once the time calibration is performed.

Using the information of the charge at the two ends of a wire, the z coordinate results to be:

$$z = A \times L_{eff} \quad (5.2)$$

where A is the charge asymmetry $\frac{Q_u - Q_d}{Q_u + Q_d}$, while L_{eff} is the effective length of the wire. Equation 5.2 can be obtained considering Figure 5.1.

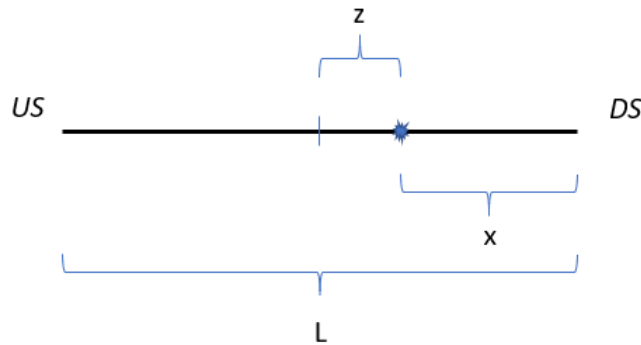


Figure 5.1. Schematic representation of a hit on a wire with the relative position used for the calculation of z with the charge division method.

Defining L as the wire length, US and DS represent the upstream and downstream read-out end, the relation between z and the distance x from DS is:

$$z = L - \left(\frac{L}{2} + x\right) = \frac{L}{2} - x \rightarrow x = L/2 - z \quad (5.3)$$

The ratio between the charges calculated by DS , Q_d and US , Q_u results from the division charge method [23]:

$$\frac{Q_d}{Q_u} = \frac{\beta x/L}{\beta + 1 - x/L} \quad (5.4)$$

with $\beta = \frac{R}{\rho L}$ where R is the input impedance of the read-out pre-amplifier circuit and ρL is the wire length multiplied for the resistivity of the wire; the entire product represents the wire resistance. The charge fraction at US is:

$$\frac{Q_u}{Q_d + Q_u} = \left(\frac{Q_d}{Q_u} + 1\right)^{-1} = \left(\frac{2\beta + 1}{\beta + 1 - x/L}\right)^{-1} \quad (5.5)$$

Expanding the equation and using the expressions of β and x :

$$\frac{Q_u}{Q_d + Q_u} = \frac{\beta + 1 - x/L}{2\beta + 1} = \frac{R/\rho L + 1 - x/L}{2R/\rho L + 1} = \frac{R + \rho(L - x)}{2R + \rho L} = \frac{R + \rho(L/2 + z)}{2R + \rho L} \quad (5.6)$$

while the charge fraction at DS results to be:

$$\frac{Q_d}{Q_d + Q_u} = 1 - \frac{Q_u}{Q_d + Q_u} = 1 - \frac{R + \rho(L - x)}{2R + \rho L} = \frac{R + \rho x}{2R + \rho L} = \frac{R + \rho(L/2 - z)}{2R + \rho L} \quad (5.7)$$

The charge asymmetry can be computed as

$$A = \frac{Q_u - Q_d}{Q_u + Q_d} = \frac{R + \rho(L/2 + z)}{2R + \rho L} - \frac{R + \rho(L/2 - z)}{2R + \rho L} = \frac{2\rho}{2R + \rho L} \cdot z \quad (5.8)$$

and the z position along the wire as a function of the charge asymmetry results

$$z = A \cdot \frac{2R + \rho L}{2\rho} \quad (5.9)$$

where the nominal value of R is 360Ω and $\rho = 175 \Omega/m$. The term $\frac{2R + \rho L}{2\rho}$ is the effective length of the wire L_{eff} and its value depends on the layer because wires belonging to different layers have different length.

5.1 Method

The aim of this analysis is to calibrate the parameters which relate the z position along the wire and the charge ratio read-out in the two ends. Equation 5.9 can be written as:

$$z = L_{eff} \frac{G \frac{Q_d}{Q_u} - 1}{G \frac{Q_d}{Q_u} + 1} \quad (5.10)$$

where G takes into account a possible difference of the gain of the two read-out electronic channels. Also the effective length L_{eff} has to be determined on data. This calibration has to be performed for each wire.

In order to determine the calibration constants an independent measurement of the z coordinate is necessary. In what follows the z coordinate calculated from the fit to the track is used (in the local coordinate system) where the wire under consideration has been removed.

The charge ratio has been expressed as a function of the z_{trk} :

$$\frac{Q_d}{Q_u} = \frac{L_{eff} + z_{trk}}{G(L_{eff} - z_{trk})} \quad (5.11)$$

The parameters G and L_{eff} have been obtained by fitting the histogram of the charge ratio Q_d/Q_u as a function of the z_{trk} shown in Figure 5.2 with the function 5.11.

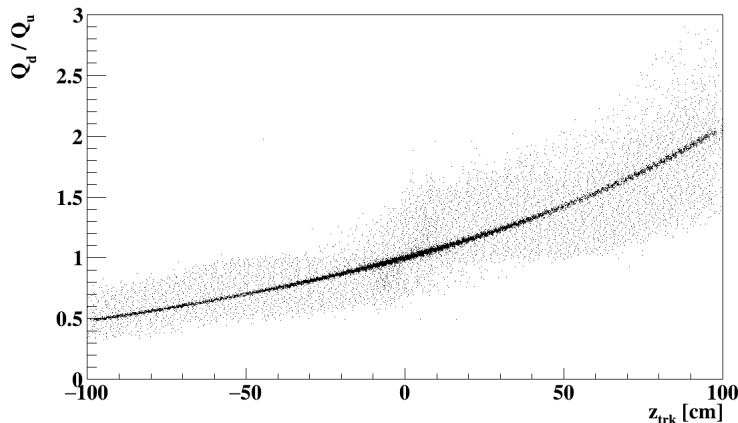


Figure 5.2. Q_d/Q_u as a function of the z_{trk} obtained considering all the wires together for a sample of 10^4 signal events.

In the Monte Carlo production the parameter G is generated equal to one, in fact each channel provides the same gain in the whole drift chamber. The L_{eff} parameter is different for each layer, because it depends on the stereo geometry. In a first step, 20 samples of 10^4 signal events have been considered and the wires with higher occupancy of the outer layer 0 (wire number in the range 40 – 80, all of which have the same L_{eff}) have been fitted separately. This corresponds to a total number of 820 samples with identical G and L_{eff} . To validate the procedure on a single

wire, a detailed study of the wire number 52 of the layer 0 has been performed. In order to perform the fit, the profile histogram of the distribution Q_d/Q_u vs z_{trk} has been realized. In the profile, the mean value of the variable Q_d/Q_u and its error are reported for each z_{trk} bin. In order to reduce the effect of the tails of the distribution, a cut has been applied before the fit. The events have been selected using the fitting function itself and imposing the following condition:

$$\frac{L_{eff} + z_{trk} - 10}{G(L_{eff} - z_{trk} + 10)} \leq \frac{Q_d}{Q_u} \leq \frac{L_{eff} + z_{trk} + 10}{G(L_{eff} - z_{trk} - 10)} \quad (5.12)$$

This cut corresponds to select the events in the band reported in Figure 5.3.

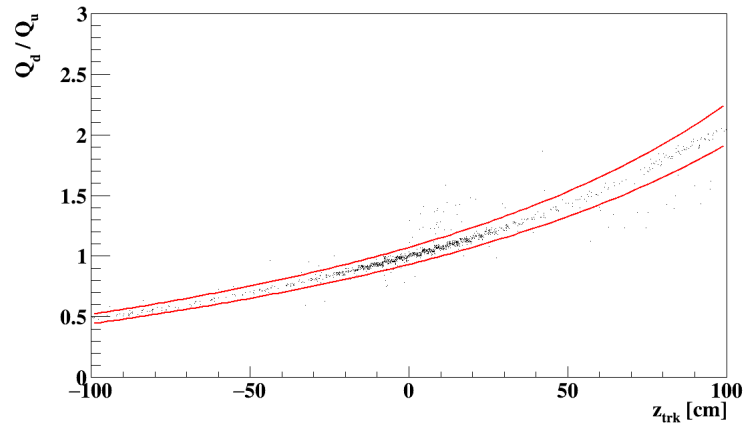


Figure 5.3. Distribution of Q_d/Q_u vs z_{trk} for the wire 52 with 10^4 signal events. The two red lines define the cut band for the event selection described in the text.

In Figure 5.4 the profile histogram (blue crosses) is shown with its fit (red line) and the charge ratio distribution (black dots) is reported in the case of wire 52 with 10^4 signal events.

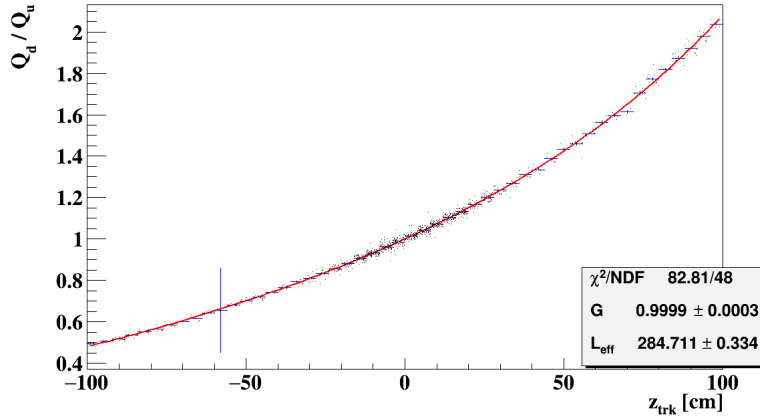


Figure 5.4. Q_d/Q_u vs z_{trk} distribution in black for the wire 52 with 10^4 signal events: the blue crosses define the profile and the red line represents the fit of the profile histogram.

5.2 Monte Carlo analysis

A study of the parameters G and L_{eff} have been realized in the 20 samples of 10^4 signal events by applying the fit procedure on the wires from the 40th to the 80th of the layer 0. Figure 5.5 shows the two distributions of the obtained fit parameters: in (a) the effective length is shown, while in (b) the gain distribution is reported. The Monte Carlo parameters, which are used for the simulation of the signal events corresponding to the layer 0 are:

$$G = 1 \quad L_{eff} = 285.155 \text{ cm} \quad (5.13)$$

Both the means of the two distributions in Figure 5.5 are compared with the Monte Carlo values in the pull distributions reported in Figure 5.6. The pull distributions are expected to be centered in zero: the mean value of the G pull distribution and L_{eff} pull distribution are respectively (-0.376 ± 0.050) and (1.379 ± 0.064) . A bias is clear in both distributions, in fact the mean value of the G pull distribution is $\sim 7.6\sigma_G$ far from the zero and the mean value of the L_{eff} pull distribution is $\sim 21.6\sigma_{L_{eff}}$ far from the zero. Both the widths of the two distributions are expected to be equal to one, instead the obtained values result higher and are 1.593 ± 0.053 for the L_{eff} pull and 1.218 ± 0.040 for the G pull.

To investigate the causes of this bias and to improve the comprehension of the Monte Carlo characteristics, a more detailed analysis has been performed increasing the statistic. One sample of $2 \cdot 10^4$ and one of $5 \cdot 10^4$ signal events without pile-up have been generated. For each of these samples, the following distributions have been studied:

- $z_{trk} - z_{true}$: z_{trk} represents the z position along the wire calculated with the positron reconstructed track, z_{true} is the true position of the hit on the wire.
- $z_{meas} - z_{true}$: z_{meas} is the hit measured position along the wire computed with the charge division method using the true value of G and L_{eff}

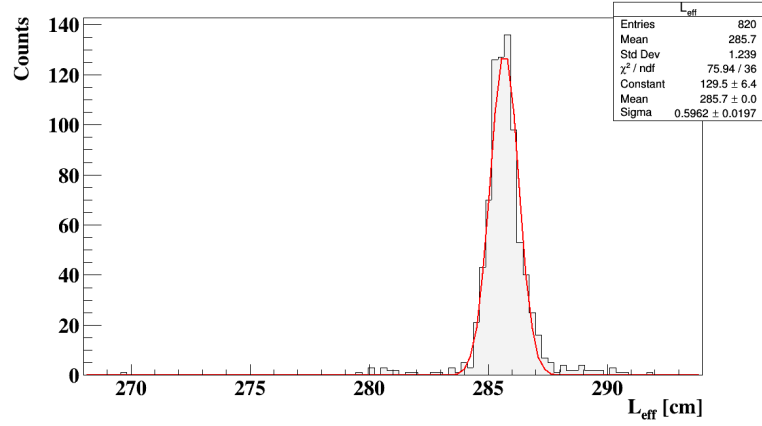
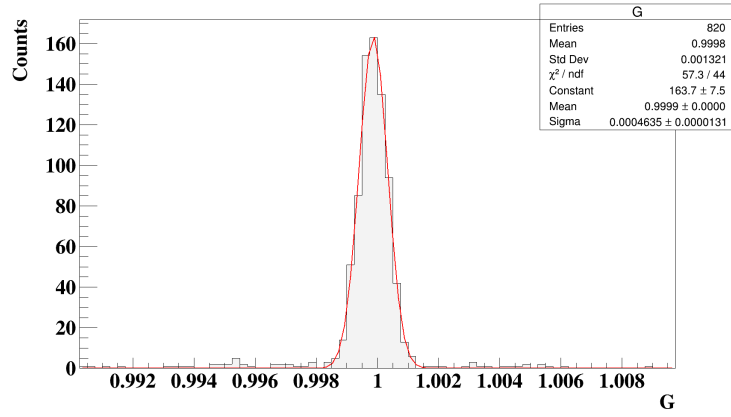
(a) L_{eff} (b) G

Figure 5.5. Distribution of the fitted L_{eff} in (a) and G in (b). The two distributions have been obtained with 20 samples of 10^4 signal events fitting the wires from 40th to 80th of the layer 0.

- $z_{meas} - z_{fit}$: z_{fit} is the z position reconstructed computed with the charge division method using the fitted values of G and L_{eff}

All these z variables are local i.e. represent the z positions in the coordinate system of the wire. While the $z_{trk} - z_{true}$ distribution provides an estimation of the track resolution, the $z_{meas} - z_{true}$ distribution is useful to evaluate the resolution of the charge division method in the limit of perfect calibration. The distribution $z_{meas} - z_{fit}$ represents the contribution of the resolution due to the calibration. The distributions obtained with the sample of 10^4 signal events for the wire 52 are reported in Figure 5.7 . A gaussian fit has been performed to these distributions and the following values of the resolutions have been obtained:

- $z_{trk} - z_{true}$ $\sigma = (0.431 \pm 0.012)$ mm
- $z_{true} - z_{meas}$ $\sigma = (1.003 \pm 0.047)$ mm

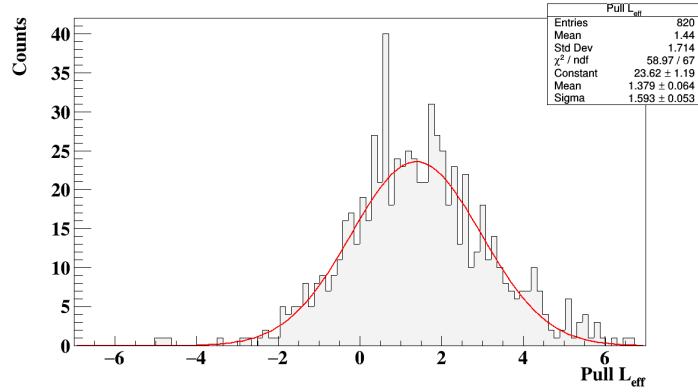
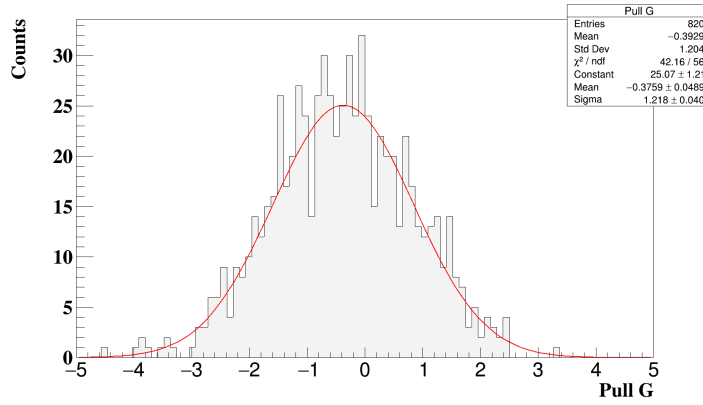
(a) $pull L_{eff}$ (b) $pull G$

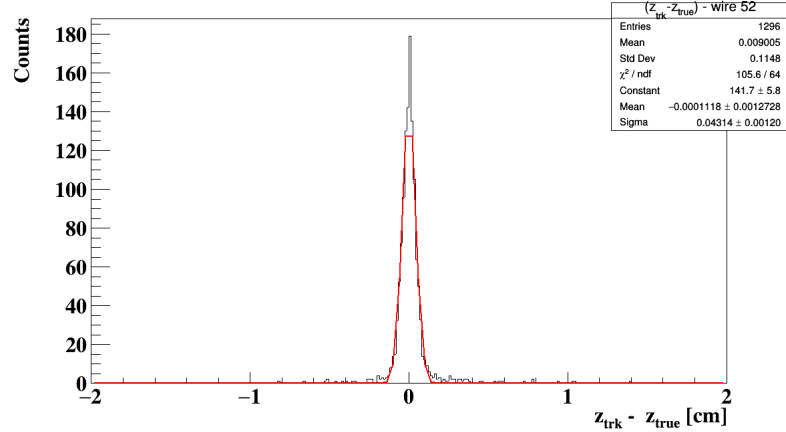
Figure 5.6. Pull distributions of the fitted L_{eff} in (a) and G in (b) for the wires 40 to 80 of the layer 0 with 20 samples of 10^4 signal events.

In Figure 5.8 the $z_{meas} - z_{fit}$ distribution is shown. The error introduced by the fit is equal to 0.145 mm . The results obtained with the samples of $2 \cdot 10^4$ and $5 \cdot 10^4$ signal events are reported in the Table 5.1. It is clear that the main source of uncertainty is the Monte Carlo resolution of the charge division method in all the cases. The contribution of the resolution due to the calibration scale as expected for the sample of $2 \cdot 10^4$ signal events. The resolution of the calibration method in the case of the sample of $5 \cdot 10^4$ signal events is currently under investigation.

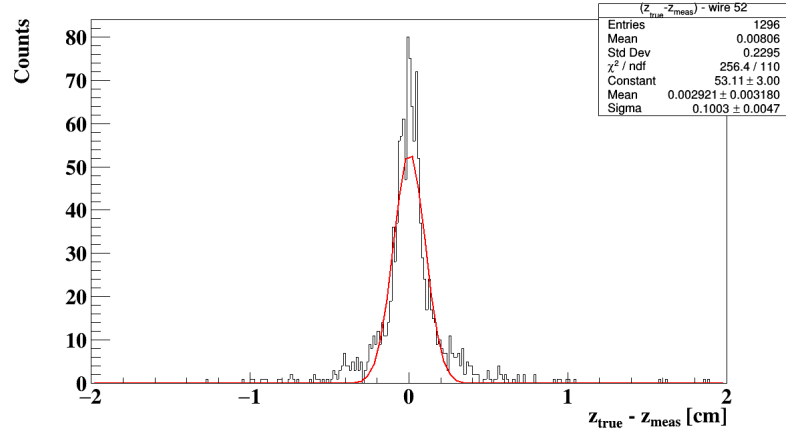
sample	$\sigma(z_{trk} - z_{true}) [mm]$	$\sigma(z_{true} - z_{meas}) [mm]$	$\sigma(z_{meas} - z_{fit}) [mm]$
10^4	0.431 ± 0.012	1.003 ± 0.047	0.145 ± 0.005
$2 \cdot 10^4$	0.422 ± 0.001	1.093 ± 0.036	0.102 ± 0.003
$5 \cdot 10^4$	0.419 ± 0.006	1.194 ± 0.023	0.393 ± 0.006

Table 5.1. Distribution widths for 10^4 , $2 \cdot 10^4$ and $5 \cdot 10^4$ signal events.

In Figure 5.9 the $\sigma(z_{meas} - z_{trk})$ as a function of z_{trk} is shown. The red line is the error introduced with the bias on the L_{eff} distribution $\sigma(z_{sys})$. This error,



(a) Track resolution



(b) Charge division method resolution

Figure 5.7. In (a) $z_{trk} - z_{true}$ distribution and in (b) $z_{meas} - z_{true}$ distributions. The two resolutions are obtained for the wire 52 with a sample of 10^4 signal events.

$\sigma(z_{sys})$, is the contribution to the resolution due to the only bias from L_{eff} and it is calculated through the uncertainties propagation:

$$\sigma(z_{sys}) = \left| \frac{\Delta L}{L} \cdot z \right| \quad (5.14)$$

where ΔL is the difference between the L_{eff} fitted value which is 284.711 cm and the true value equal to 285.155 cm . The only error propagated is the one of the L_{eff} , meanwhile the G parameter is fixed to one. This choice is reasonable, in fact the G is fitted better than the L_{eff} and the bias of the effective length is much bigger. This implies that for a hit in $z = 100 \text{ cm}$ the uncertainty is equal to $\sigma(z_{sys}) \simeq 0.156 \text{ cm}$.

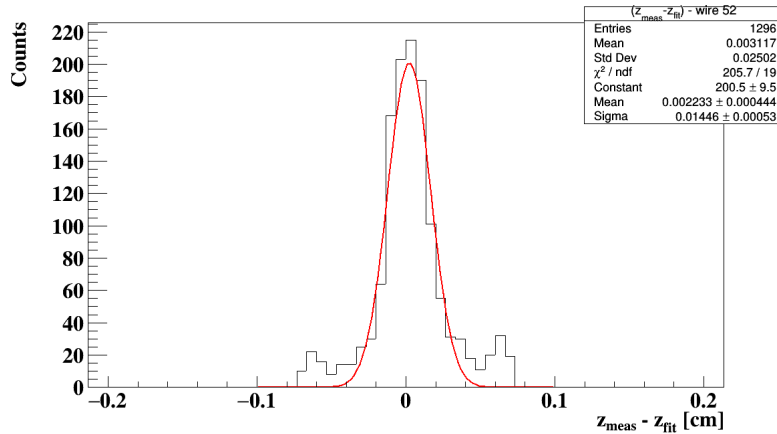


Figure 5.8. Contribution of the calibration to the resolution: the distribution of $(z_{meas} - z_{fit})$ is obtained for the wire 52 with a sample of 10^4 signal events.

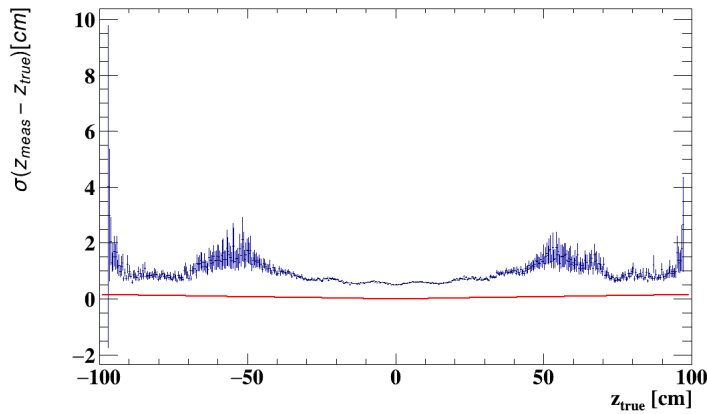


Figure 5.9. $\sigma(z_{meas} - z_{trk})$ vs z_{trk} distribution. The red line represents $\sigma(z_{sys})$. The error $\sigma(z_{sys})$ introduced with the bias on the L_{eff} is less than the others.

Thus, the method developed to calibrate the charge division, with a statistics of ~ 1300 hits on a wire is adequate to make the contribution of the calibration negligible with respect to the intrinsic resolution of the charge division method, despite the bias on the fitted parameters. However, this bias is currently under investigation.

Chapter 6

Data Analysis

The time calibration method developed in 4.1.3 has been tested on data from cosmic rays taken by a small monitoring drift chamber which is currently installed in the MEGII gas system to monitor the quality of the helium-isobutane ($He : i - C_4H_{10}$) mixture. The properties of this chamber have been studied in laboratory using different sources, in particular cosmic muons. In this chapter, the monitoring drift chamber is briefly presented, the collected data and the method used for the analysis are shown with the obtained results.

6.1 Monitoring Drift Chamber

The monitoring drift chamber is composed by two layers of 16 Mylar tubes of 1 cm diameter (staggering 0.5 cm) and 37 μm thick. Each tube has a cylindrical shape and a gold-plated tungsten wire of 20 μm is placed on its axis. The detector is filled with a gas mixture of 85 : 15 $He : i - C_4H_{10}$. The drift chamber operates at ~ 1600 V. The signal from the sense wires is amplified by custom pre-amplifiers and then is collected and digitized by two 4-channel Domino Ring Sampler (DRS) boards and an oscilloscope. A picture of the drift chamber is reported in Figure 6.1. The

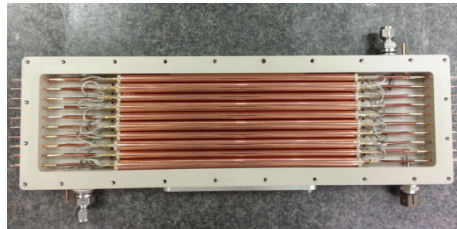


Figure 6.1. Picture of the opened drift chamber.

position of the tubes and the number associated with them in the read-out scheme is shown in Figure 6.2. The signal is read-out on only one side of the chamber. One of the channel has been used to produce a trigger signal for the others.

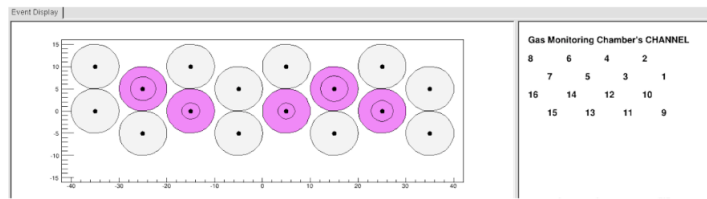


Figure 6.2. Schematic picture of the sense wires in the drift chamber.

6.2 Method

The number of muon events used for this analysis is 36949. The coincidence of two plastic scintillators have been used to provide a trigger for the cosmic muons data taking: the first was placed under the drift chamber and the second on top of the drift chamber. The constant fraction method has been applied to calibrate the times of the different wires. A time distribution has been realized for each tube. In Figure

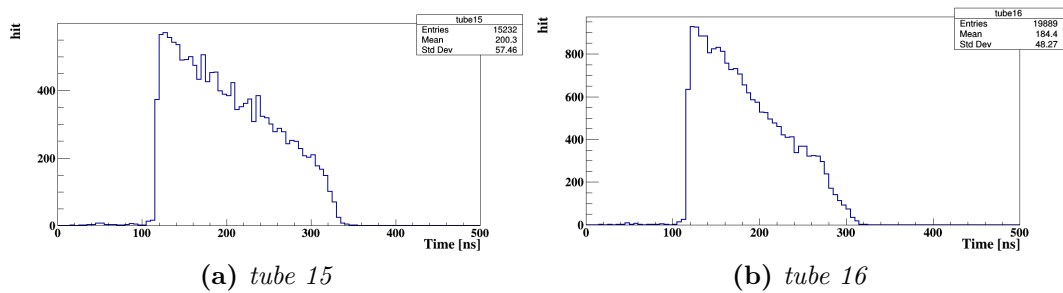


Figure 6.3. Reconstructed hit time distribution for the tubes 15 and 16 of the monitoring drift chamber obtained with cosmic muons.

6.3 the distributions of the hit time obtained from the tubes 16 and 15 are shown. The time distributions from the other tubes are reported in Appendix D.

The threshold method has been used to determine the edge time. The edge time represents the offset between the electronic channel and the trigger channel. The threshold used is equal to the 15% of the maximum peak.

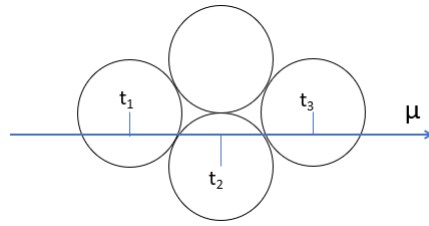


Figure 6.4. Sketch of an atmospheric muon crossing the tubes of the gas monitoring drift chamber. t_1, t_2, t_3 represent the time of the signals read-out in each tube.

6.3 Results

In Table 6.1 the time calibration constants are reported.

tube	Edge time [ns]
1	113.587
2	84.135
3	13.250
4	81.303
5	113.542
6	82.764
7	84.433
8	83.613
9	84.283
10	39.861
11	85.052
12	88.181
13	50.250
14	109.552
15	113.475
16	113.431

Table 6.1. Time calibration constants for each tube.

Two typical values can be noticed: one is ~ 110 ns and the other is ~ 84 ns. These values regroup the two different read-out electronics used, in fact ~ 110 ns is associated with the oscilloscope, meanwhile ~ 84 ns is that for the DRS digitizer. The distributions of the tubes 3, 10 and 13 are not well defined and this reason the offset constants result incompatible with the others. This is caused by the low number of the hits in these tubes.

A procedure to check the validity of the calibration constants determined has been implemented. In fact, considering four tubes placed as in Figure 6.4, the three variables t_1 , t_2 and t_3 represent the times in which the signal is read-out in each tube. If the drift velocity is considered constant in the whole tube, the following distribution is constant too

$$\frac{t_1 + t_3}{2} + t_2 = \text{constant} = \frac{v}{d} \quad (6.1)$$

where v is the drift velocity and d represents the vertical distance between the track and the sense wire.

The same distribution can be realized using the central upper tube in the same figure. It is expected that the two distributions overlap. The two following distributions have been realized

$$T_1 = \frac{t_1 + t_3}{2} + t_2; \quad T_2 = \frac{t_1 + t_3}{2} + t_4 \quad (6.2)$$

where t_4 is the time in the upper tube. The tubes 7, 14, 15 and 16 have been chosen for this analysis. The events with a hit in the triplet (14,15,16) or in the triplet (14,7,16) have been selected, obtaining the distributions in Figure 6.5. The two

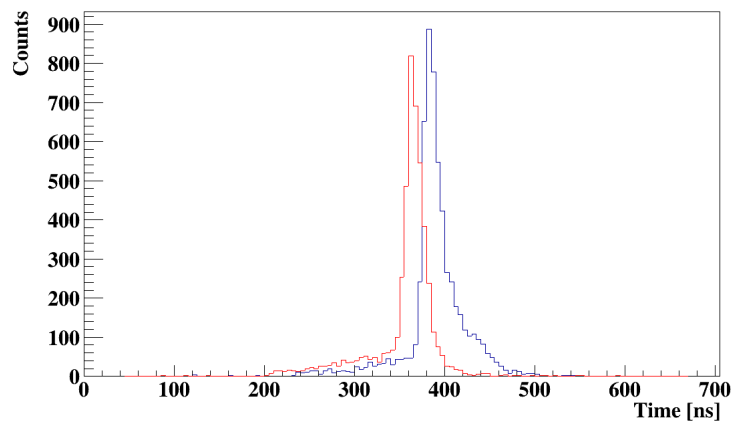


Figure 6.5. Time distributions T_1 and T_2 before the time calibration. The black line distribution is obtained with the triplet (14,15,16), while the red the distribution with the triplet (14,7,16).

distribution are clearly separated, in fact the distance between the two peaks is around 20 ns . This clear separation in time of the peaks is caused by the different read-out electronics of the channels, in fact, the channel 7 is read-out by a DRS, meanwhile the channel 15 is read-out with the oscilloscope.

After the calculation of the calibrations with the constant threshold method, the time constants have been subtracted to the data and a new plot of these two distributions has been obtained in Figure 6.6. After the calibration the two peaks coincide, a difference of ~ 4 ns remains.

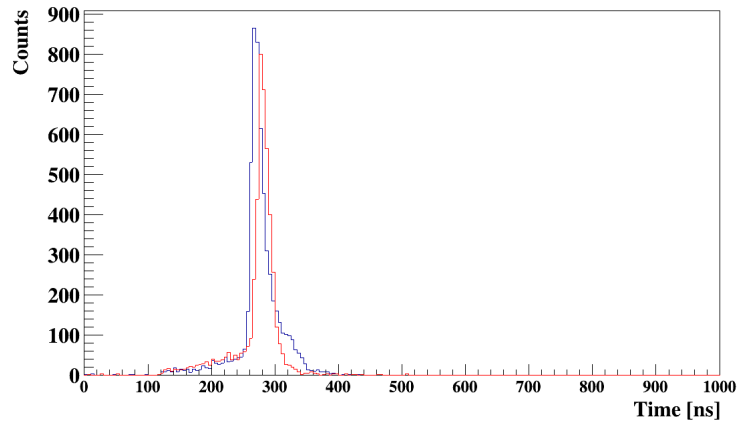


Figure 6.6. Time distribution after the calibration: in black T_1 and in red T_2 .

Chapter 7

Conclusions

In this thesis, the time and charge calibration of the MEGII drift chamber have been studied. The MEGII DCH is a unique volume low-mass detector with a high granularity and a stereo wires configuration. A high precision in the measurement of the positron momentum, production time and angle is required. Moreover, the time calibration algorithm has been tested using cosmic muons data.

The first part of the analysis, two different methods have been studied: the template fit method and the constant fraction method. For both of them, a stability test has been performed using different statistics. The template fit method has emerged as being unstable and the obtained results were not satisfying. Instead, the constant fraction method resulted to be efficient and a good error on the time calibration constant has been obtained for different sizes of the simulated data. Considering a trigger acquisition rate of 10 Hz, it has been evaluated the DAQ time necessary for a precision of 500 *ps* in the measurement of the calibration constants. It is possible to reach the above-mentioned precision for the calibration constants for each wire with a data taking time between 41 hours up to 158 depending on the wire position. The second part of the analysis has been focused on the study of the *z* position reconstructed with the charge division method. The distribution of the charge ratio as a function of the *z* position reconstructed with the track has been fitted with the function of the charge division method. The fit has been performed on Monte Carlo simulated events on the wires with the highest occupancy. The precision of the charge division has been studied and its contribution to the resolution has been compared to the intrinsic resolution. It has been found an uncertainty introduced by the fit that is $(0.145 \pm 0.005 \text{ mm})$ lower than the uncertainty due to the Monte Carlo resolution $(1.003 \pm 0.047 \text{ mm})$.

In the third part of the thesis, the constant fraction method has been tested on cosmic muons data collected with the gas monitoring drift chamber of the MEGII experiment. The monitoring drift chamber is composed by 16 drift tubes and two different tools has been used for the read-out of the signal from the sense wires: an oscilloscope and a DRS waveform sampler. The time calibration constants have been determined for each channel. The time distributions with the tracks traversing three adjacent tubes has been realized and aligned. The distance between the peaks of each distribution has been reduced from a starting value of $\sim 20 \text{ ns}$ to a final value of 4 *ns*.

The studied algorithms resulted all valid and a more detailed analysis would be interesting in order to better understand the issues found with the template fit method or to examine in depth the charge division method using higher simulated data size. The MEGII drift chamber is going to be operative and it will be soon possible to test the studied algorithms comparing the Monte Carlo simulated events analysis with the data analysis.

Appendix A

Template fit parameters: samples of $2.5 \cdot 10^4$ and $5 \cdot 10^4$ signal events.

The figures reported here are the fitted offset parameter and the scale factor as a function of the end obtained with the samples of $2.5 \cdot 10^4$ and $5 \cdot 10^4$ signal events.

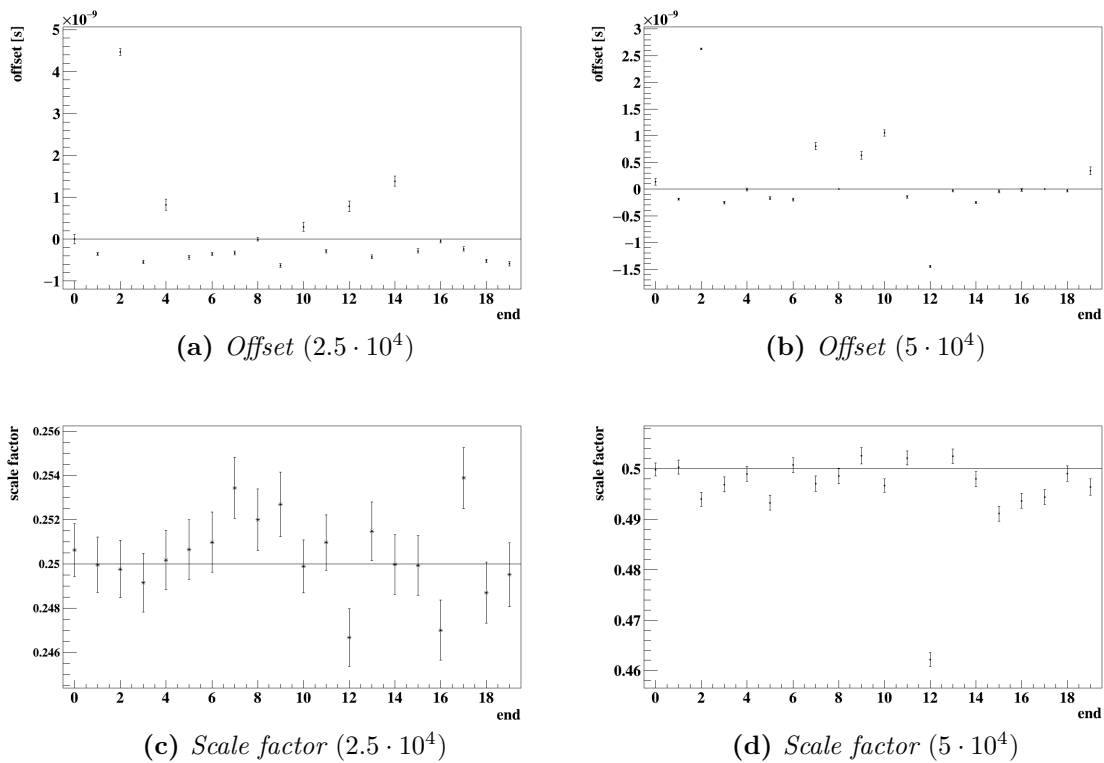
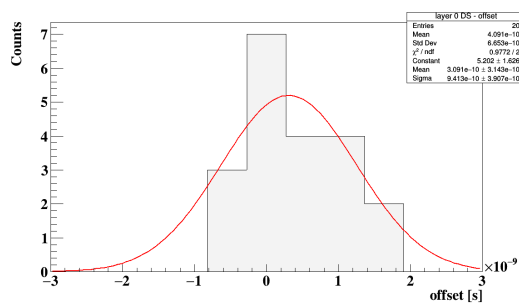


Figure A.1. Offset parameter and scale factor as a function of the end: in (a) and in (c) are fitted with the sample of $2.5 \cdot 10^4$ simulated events, while in (b) and in (d) with the sample of $5 \cdot 10^4$ simulated events. The black line represents the expected value of the fitted parameters.

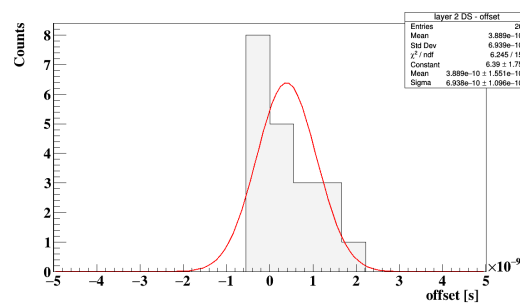
Appendix B

Template fit parameters distributions

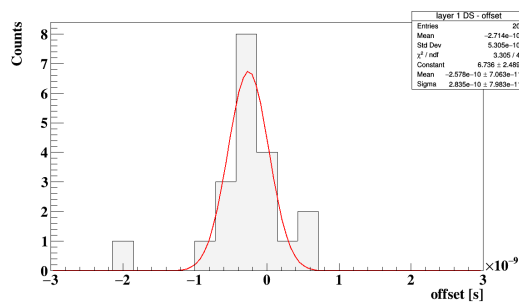
The following figures illustrate the fitted offset parameter and scale factor distributions obtained with the template fit for each layer from the DS end on a sample of 10^4 simulated signal events.



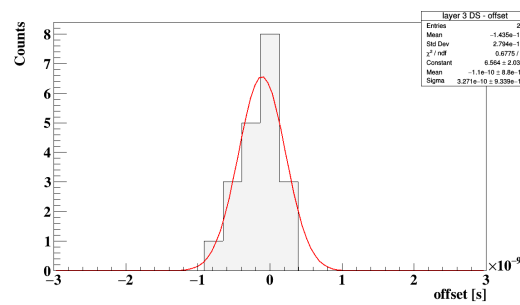
layer 0 DS



layer 2 DS



layer 1 DS



layer 3 DS

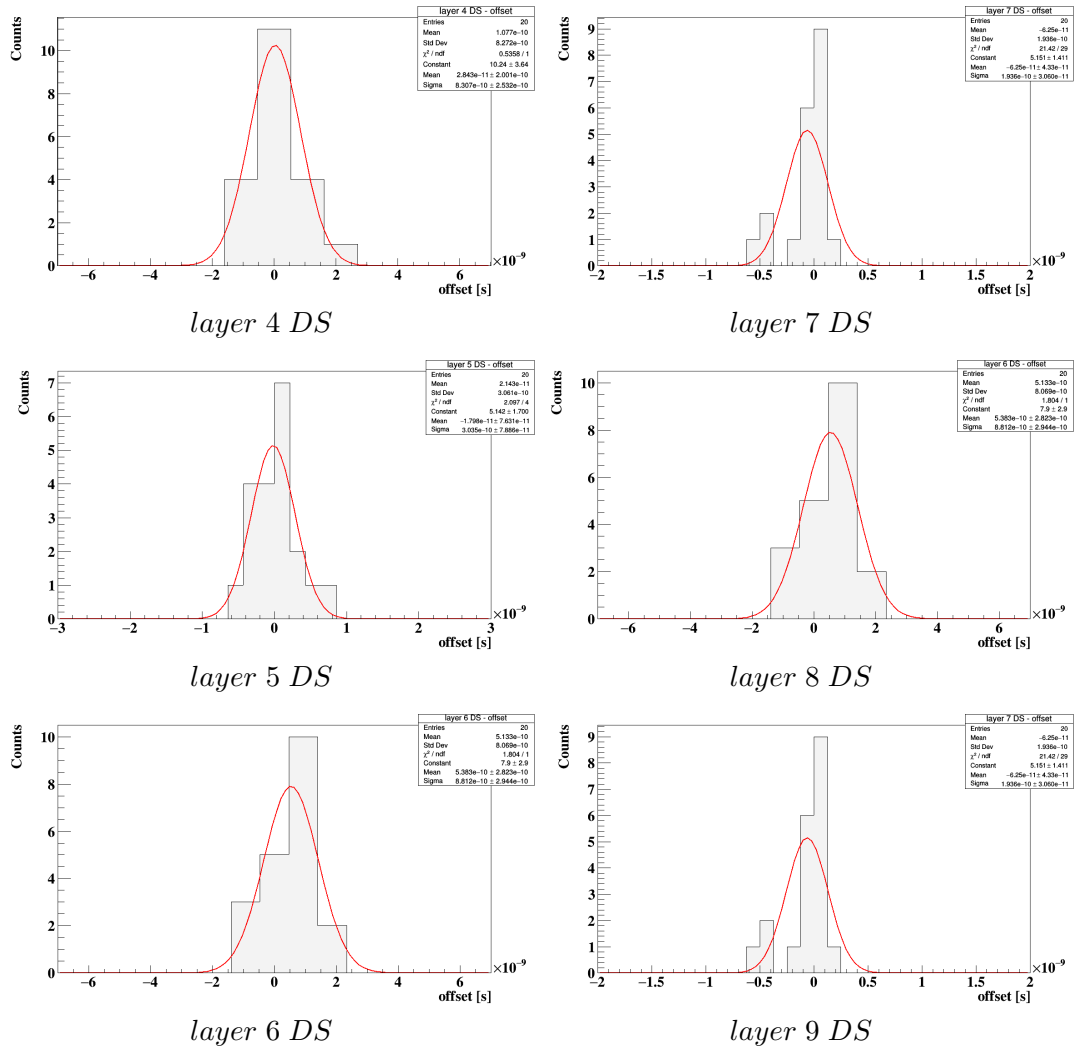


Figure B.1. Fitted offset parameter distribution for DS read-out of each layer for 10^4 signal events. A gaussian fit is performed.

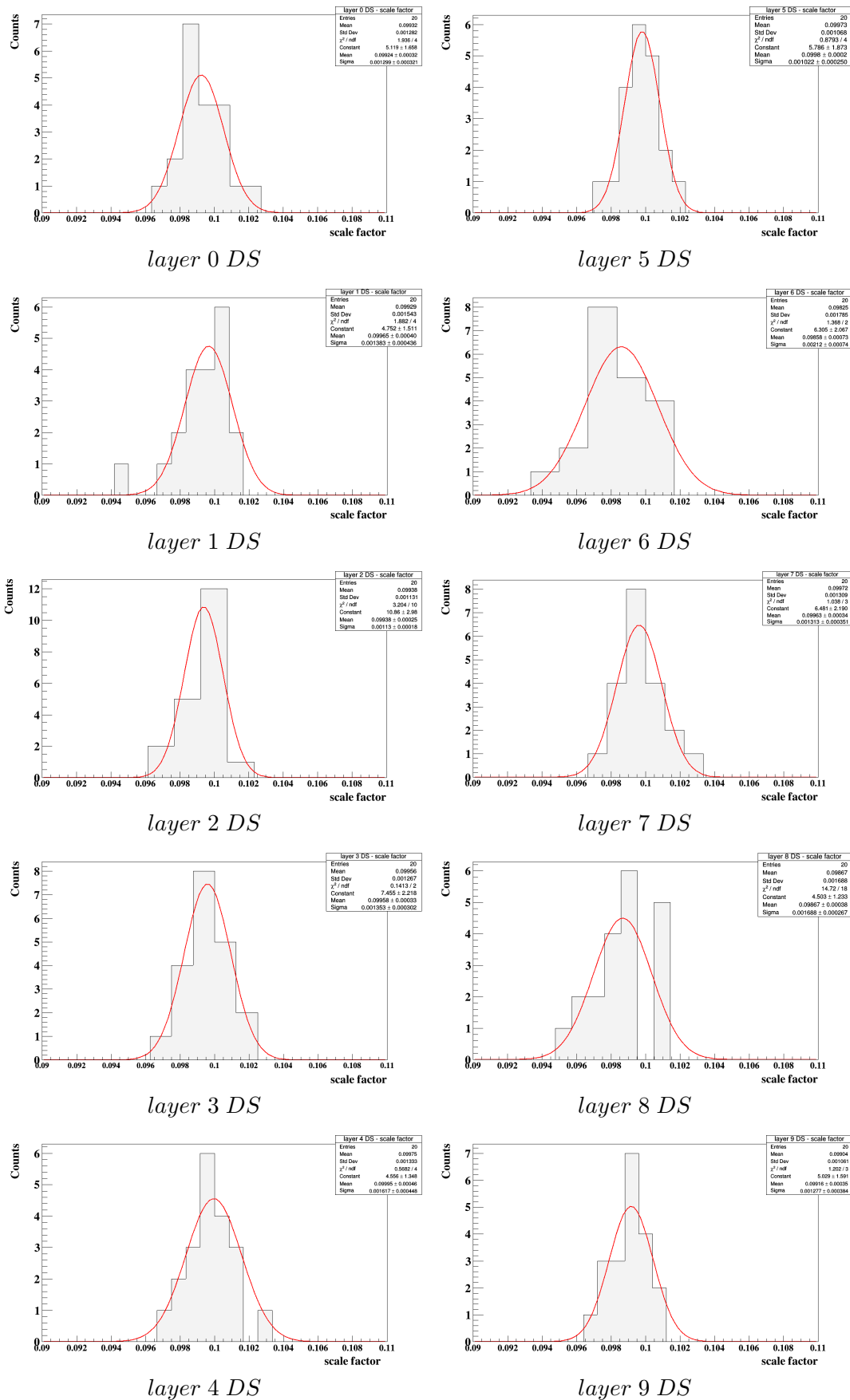
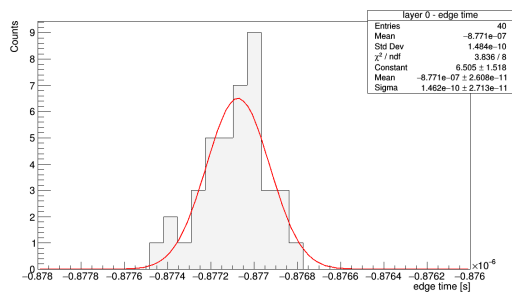


Figure B.2. Fitted scale factor distribution for DS read-out of each layer for 10^4 signal events. A gaussian fit is superimposed.

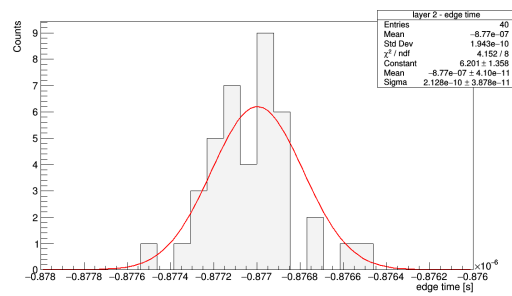
Appendix C

Constant fraction method parameters distributions

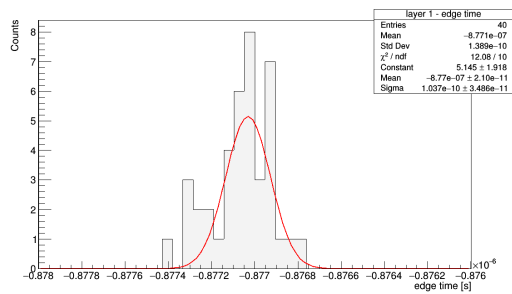
The following histograms show the edge time distributions obtained for each layer with the constant fraction method. These distributions are obtained with the samples of 10^4 signal events.



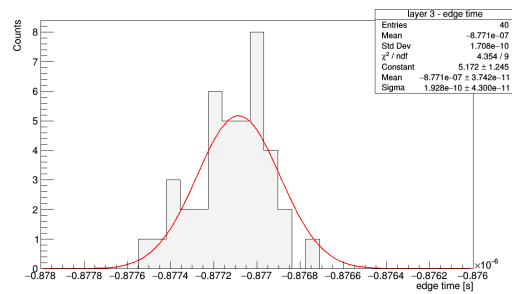
layer 0



layer 2



layer 1



layer 3

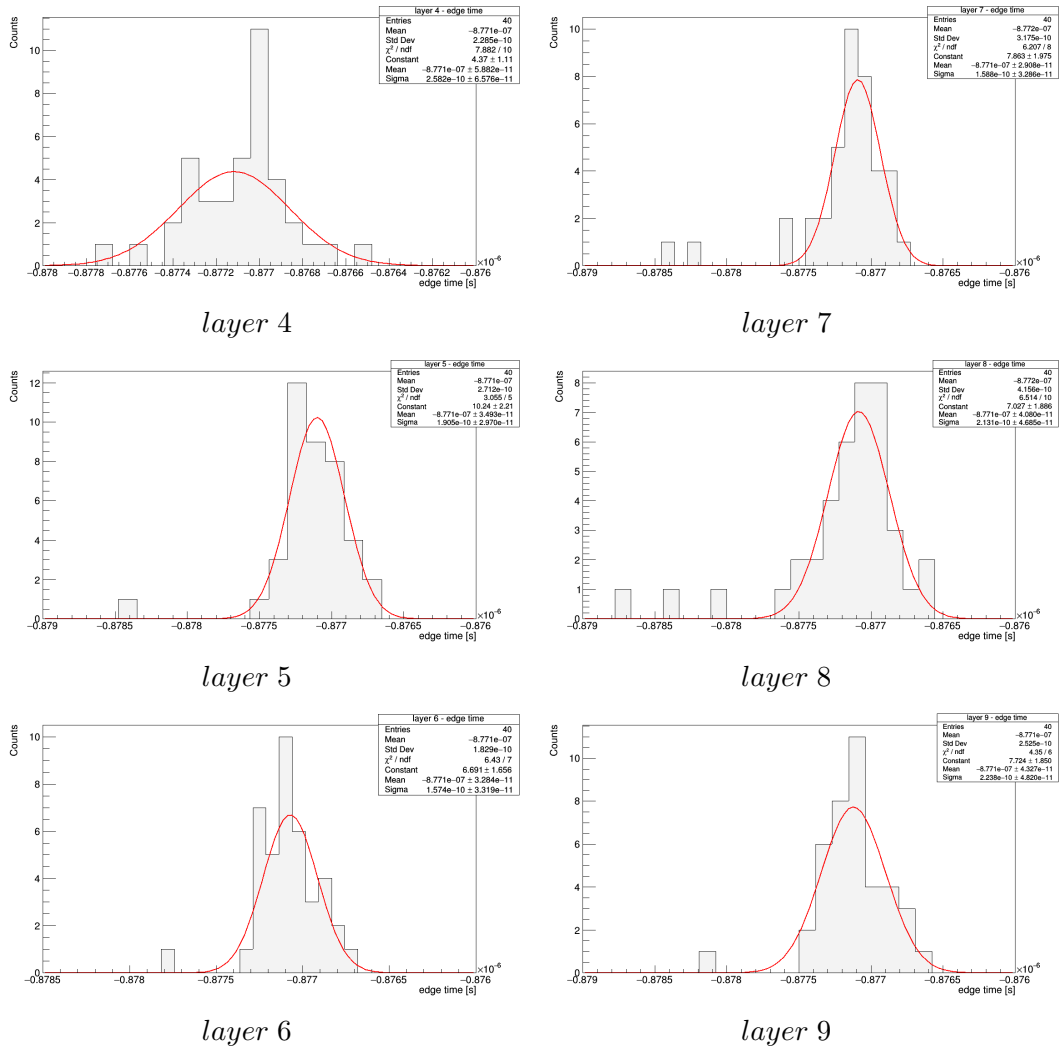
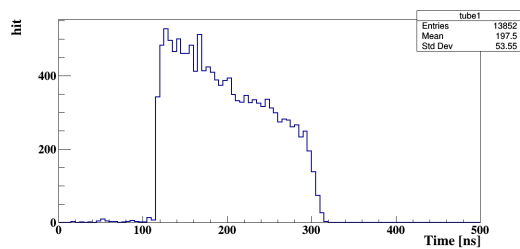


Figure C.1. Edge time distribution obtained from the constant fraction method per layer for 10^4 signal events. A gaussian fit is superimposed.

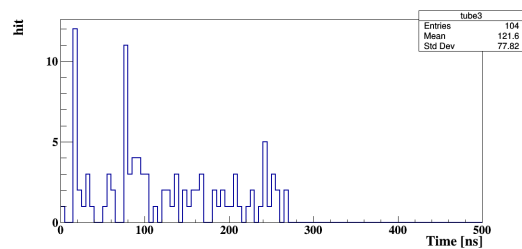
Appendix D

Drift time distribution from the gas monitoring drift chamber.

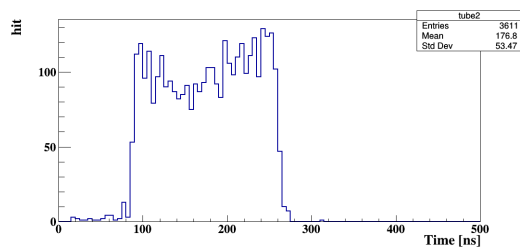
The drift time distribution for each tube of the monitoring drift chamber obtained with the cosmic muons data are reported here.



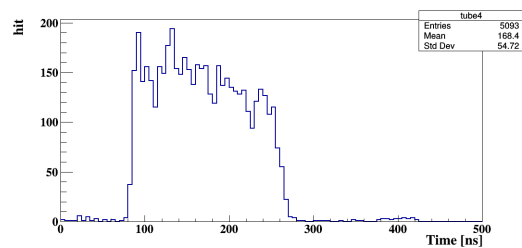
tube 1



tube 3



tube 2



tube 4

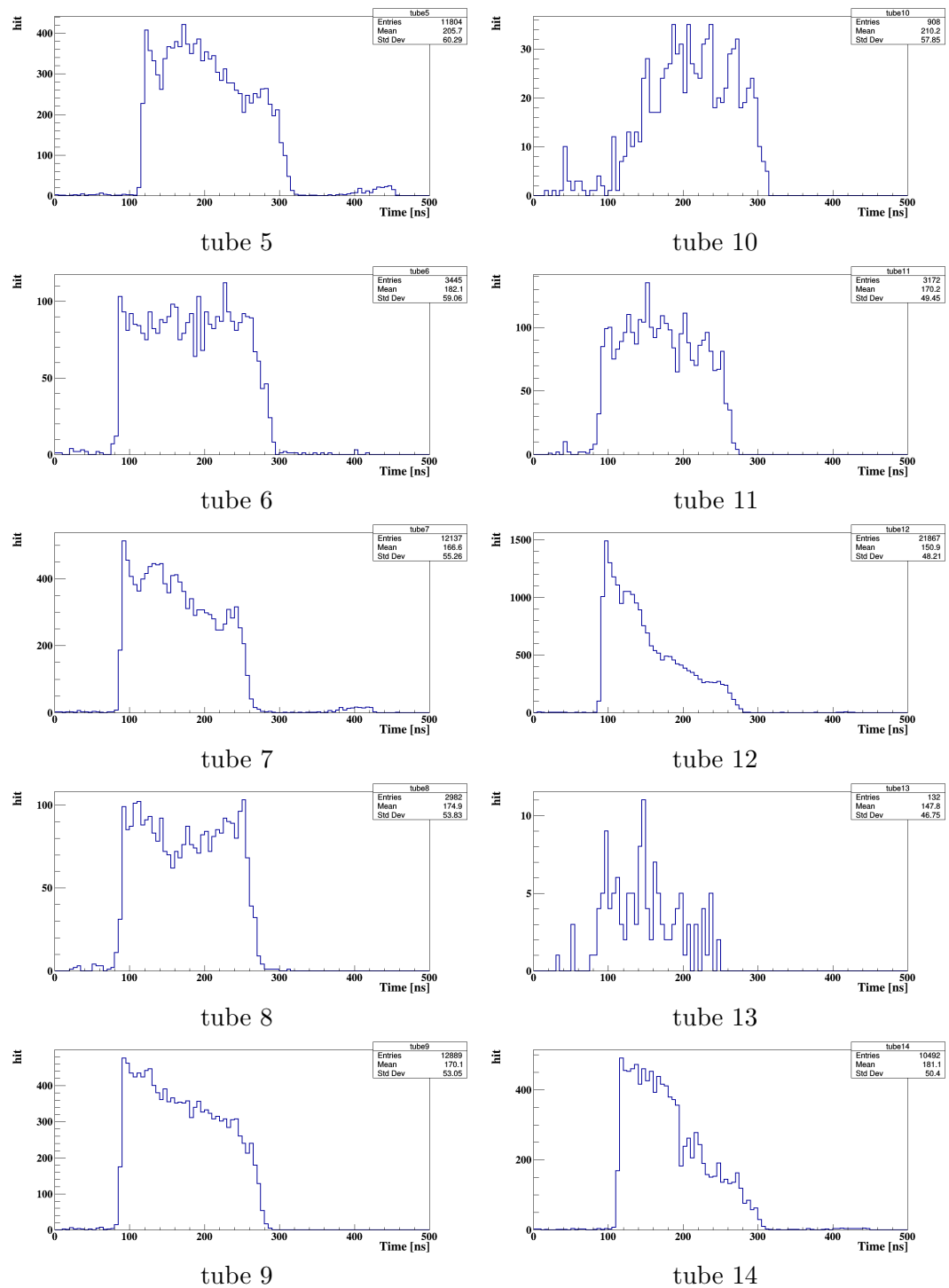


Figure D.1. Drift time distribution for each tubes of the monitoring drift chamber obtained with cosmic muons data.

Bibliography

- [1] Takaaki Kajita for the Super-Kamiokande and Kamiokande collaborations. Atmospheric neutrino results from super-kamiokande and kamiokande - evidence for ν_μ oscillations. *arXiv:hep-ex/9810001*, 1998.
- [2] Particle Data Group. Review of particle physics.
- [3] E. P. Hincks and B. Pontecorvo. On the absence of photons among the decay products of the 2.2-microsecond meson. *Can. J. Res. 28A, 29 (1950)*, reprinted in S. M. Bilenky et al. (editors) “Bruno Pontecorvo” Società Italiana di Fisica, 1997.
- [4] A. M. Baldini et al. [MEG Collaboration]. Search for the lepton flavour violating decay $\mu^+ \rightarrow e^+\gamma$ with the full dataset of the meg experiment. *Eur. Phys. J. C 76 no.8, 434 [arXiv:1605.05081 [hep-ex]]*, 2016.
- [5] P. Depommier et al. A new limit on the $\mu^+ \rightarrow e^+\gamma$ decay. 1977.
- [6] A. van der Schaaf, R. Engfer, H. P. Povel, W. Dey, H. K. Walter, and C. Petitjean. A search for the decay $\mu^+ \rightarrow e^+\gamma$. *Nucl. Phys. A 340, 249*, 1980.
- [7] W. Kinnison et al. A search for $\mu^+ \rightarrow e^+\gamma$. *Phys. Rev. D 25, 2846*, 1982.
- [8] R. D. Bolton et al. Search for rare muon decays with the crystal box detector. *Phys. Rev. D 38 2077*, 1988.
- [9] M. Ahmed et al. Search for the lepton-family-number nonconserving decay $\mu^+ \rightarrow e^+\gamma$. *Phys. Rev. D 65 112002*, 2002.
- [10] L. Calibbi and G. Signorelli. “charged lepton flavor violation: An experimental and theoretical introduction”. [*arXiv:1709.00294*], 2017.
- [11] U. Bellgardt et al. [SINDRUM Collaboration]. Search for the decay $\mu^+ \rightarrow e^+e^-e^+$. *Nucl. Phys. B 299*, 1988.
- [12] A. Blondel et al. Research proposal for an experiment to search for the decay $\mu \rightarrow eee$. [*arXiv:1301.6113 [physics.ins-det]*], 2013.
- [13] W.H. Bertl et al. [SINDRUM II Collaboration]. A search for muon to electron conversion in muonic gold. *Eur. Phys. J. C 47 337*, 2006.
- [14] A. Kurup. The coherent muon to electron transition (comet) experiment. *Nuclear Physics B-Proceedings Supplements, 218(1):38-43*, 2011.

- [15] D. Glenzinski. The mu2e experiment at fermilab. *in AIP Conference Proceedings, volume 1222, pages 383–386. AIP*, 2010.
- [16] S.E. Csorna et al. [CLEO Collaboration]. Update of the search for neutrinoless decay $\tau \rightarrow \mu\gamma$. *Phys. Rev. D* **61** 071101, 2000.
- [17] B. Aubert et al. [BABAR Collaboration]. Searches for lepton flavor violation in the decays $\tau^\pm \rightarrow e^\pm\gamma$ and $\tau^\pm \rightarrow \mu^\pm\gamma$. *Phys. Rev. Lett.*, **104**:021802, 2010.
- [18] K. Hayasaka et al. Search for lepton-flavor-violating τ decays into three leptons with 719 million produced $\tau^+\tau^-$ pairs. *Physics Letters B*, **687**(2):139–143, 2010.
- [19] Y. Ahmis et al. Averages of b -hadron, c -hadron and τ -lepton properties as of summer 2016. *arXiv:1612:07233[hep-ex]*, 2016.
- [20] A. M. Baldini, E. Baracchini, G. Cavoto, M. Cascella, F. Cei, M. Chiappini, G. Chiarello, C. Chiri, S. Dussoni, L. Galli, F. Grancagnolo, M. Grassi, V. Martinelli, D. Nicolò, M. Panareo, A. Pepino, G. Piredda, F. Renga, E. Ripiccini, G. Signorelli, G.F. Tassielli, F. Tenchini, M. Venturini, and C. Voena. Single-hit resolution measurement with meg ii drift chamber prototypes. *arXiv:1605.07970 [physics.ins-det]*, 2016.
- [21] Geant4. <https://geant4.web.cern.ch/geant4/>.
- [22] Rene Brun and Fons Rademakers. Proceedings aihenp’96 workshop, lausanne. *Nucl. Inst. and Meth. in Phys. Res. A* **389** (1997) 81-86. See also [root.cern.ch/] (<http://root.cern.ch/>), 1996.
- [23] Luigi Rolandi, Werner Riegler, and Walter Blum. Particle detection with drift chamber. *Springer*, 2008.